



January 2019

## Comparison Of Backscatter Coefficients For Airborne Cloud Probes

Shawn Wendell Wagner

Follow this and additional works at: <https://commons.und.edu/theses>

---

### Recommended Citation

Wagner, Shawn Wendell, "Comparison Of Backscatter Coefficients For Airborne Cloud Probes" (2019).  
*Theses and Dissertations*. 2873.  
<https://commons.und.edu/theses/2873>

This Thesis is brought to you for free and open access by the Theses, Dissertations, and Senior Projects at UND Scholarly Commons. It has been accepted for inclusion in Theses and Dissertations by an authorized administrator of UND Scholarly Commons. For more information, please contact [zeineb.yousif@library.und.edu](mailto:zeineb.yousif@library.und.edu).

COMPARISON OF BACKSCATTER COEFFICIENTS FOR  
AIRBORNE CLOUD PROBES

by

Shawn Wagner  
Bachelor of Science, University of North Dakota, 2016

A Thesis  
Submitted to the Graduate Faculty  
of the  
University of North Dakota  
in partial fulfillment of the requirements

for the degree of  
Master of Science

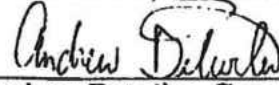
Grand Forks, North Dakota  
December  
2019

Copyright 2019 Shawn Wagner

This thesis, submitted by Shawn Wagner in partial fulfillment of the requirements for the Degree of Master of Science from the University of North Dakota, has been read by the Faculty Advisory Committee under whom the work has been done and is hereby approved.



David Delene, Committee Chair

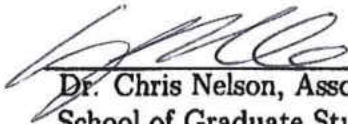


Andrew Detwiler, Committee Member



Mark Ray, Committee Member

This thesis is being submitted by the appointed advisory committee as having met all of the requirements of the School of Graduate Studies at the University of North Dakota and is hereby approved.



Dr. Chris Nelson, Associate Dean  
School of Graduate Studies

12/10/19  
DATE

## PERMISSION

Title	Comparison of Backscatter Coefficients for Airborne Cloud Probes
Department	Atmospheric Sciences
Degree	Master of Science

In presenting this thesis in partial fulfillment of the requirements for a graduate degree from the University of North Dakota, I agree that the library of this University shall make it freely available for inspection. I further agree that permission for extensive copying for scholarly purposes may be granted by the professor who supervised my thesis work or, in her absence, by the Chairperson of the department or the dean of the School of Graduate Studies. It is understood that any copying or publication or other use of this thesis or part thereof for financial gain shall not be allowed without my written permission. It is also understood that due recognition shall be given to me and to the University of North Dakota in any scholarly use which may be made of any material in my thesis.

Shawn Wagner  
December 4, 2019

## TABLE OF CONTENTS

LIST OF FIGURES . . . . .	<b>vi</b>
LIST OF TABLES . . . . .	<b>xi</b>
ACKNOWLEDGMENTS . . . . .	<b>xii</b>
ABSTRACT . . . . .	<b>xiii</b>
CHAPTER	
1 INTRODUCTION . . . . .	<b>1</b>
2 BACKGROUND . . . . .	<b>3</b>
2.1 Ice Particle Icing . . . . .	3
2.2 Cloud Probes . . . . .	5
3 AIRCRAFT MEASUREMENTS . . . . .	<b>9</b>
3.1 Ice Particle Formation . . . . .	11
4 METHODOLOGY . . . . .	<b>13</b>
4.1 Data Processing . . . . .	13
4.2 Probe Equations . . . . .	18
4.3 Light Scattering . . . . .	19
5 DATA SET . . . . .	<b>23</b>
6 RESULTS AND DISCUSSION . . . . .	<b>28</b>
7 CONCLUSIONS . . . . .	<b>37</b>
APPENDIX . . . . .	<b>38</b>
REFERENCES . . . . .	<b>43</b>

## LIST OF FIGURES

Figure		Page
1	Side view illustration showing the general features of an optical array probe, which images cloud particles as the probe moves forward (black arrows) through the air. Ice crystals (indicated in blue) encounter the laser beam (red lines) which passes through the optical windows (light gray boxes) and block the light emitted by the laser beam generator (green box). Heated, anti-shattering tips (orange triangles) prevent ice build up and reduce broken particles falling into the depth of field (dark gray rectangle). Images are recorded of the photodiode array elements (purple oval) when at least one element is reduced in intensity by 50 % . The sampling of the array elements is synchronized to the air speed of the probe to create a two-dimensional image. . . . .	6
2	Image showing the North Dakota Citation II Research Aircraft and instrumented pylons as configured for the Florida 2015 campaign. The optical window used by the Optical Ice Detector (OID) is shown in the upper left, which is angled slightly so the sampling region is in front of, and level with, the wing (labeled “OID Sample Volume”). The Cloud Droplet Probe (CDP) is used for measuring cloud droplets with the smallest of the diameters. The 2 Dimensional Cloud probe (2D-C) uses a 32-photodiode array of 30 $\mu\text{m}$ elements. The 2 Dimensional Stereo (2D-S) probe uses two linear 128 photodiode arrays and the High Volume Precipitation Spectrometer Version 3 (HVPS3) a single linear 128-photodiode array to sample particles in the mid-size diameter range and the large diameter range, respectively. The Nevzorov Probe is a hot-wire probe used to measure the liquid water content, ice water content, and total water content. . . . .	10

3	Plot showing the altitude (black) and air temperature (blue) sampled during the North Dakota Citation II Research Aircraft’s flight on 02 August 2015 (+10 °C case). Measurements focused on high altitude anvil cirrus clouds produced by intense convection. The red rectangle indicates the time segment (69,510 – 69,570 s from midnight UTC) analyzed, where the average altitude is 3,400 m GPS and the average temperature is 10 °C. The center panels contain 2D-S images from the analyzed time. . . . .	24
4	Plot showing the altitude (black) and air temperature (blue) sampled during the North Dakota Citation II Research Aircraft’s flight on 01 August 2015 (+5 °C case). Measurements focused on high altitude anvil cirrus clouds produced by intense convection. The red rectangle indicates the time segment (57,850 – 57,910 s from midnight UTC) analyzed, where the average altitude is 3,400 m GPS and the average temperature is 5 °C. The center panels contain 2D-S images from the analyzed time. . . . .	25
5	Plot showing the altitude (black) and air temperature (blue) sampled during the North Dakota Citation II Research Aircraft’s flight on 31 July 2015 (-35 °C case). Measurements focused on high altitude anvil cirrus clouds produced by intense convection. The red rectangle indicates the time segment (71,710 – 71,770 s from midnight UTC) analyzed, where the average altitude is 9,475 m GPS and the average temperature is -35 °C. The center panels contain 2D-S images from the analyzed time. . . . .	26
6	Plot showing the altitude (black) and air temperature (blue) sampled during the North Dakota Citation II Research Aircraft’s flight on 01 August 2015 (-45 °C case). Measurements focused on high altitude anvil cirrus clouds produced by intense convection. The red rectangle indicates the time segment (72,700 – 72,760 s from midnight UTC) analyzed, where the average altitude is 11,000 m GPS and the average temperature is -45 °C. The center panels contain 2D-S images from the analyzed time. . . . .	27



7	Plots showing results for the +10 °C case (15_08_02_18_23_48). The probe measured total concentrations versus time can be seen in the upper left, the cloud probes measured mean particle diameter versus time in the upper center, the calculated backscatter coefficient versus the particle diameter in the upper right, the cloud probes measured particle size spectrum (normalized by bin width and particle diameter) in the lower left, the Optical Ice Detector (OID) measured backscatter coefficients with the derived backscatter coefficients versus time on the y-axis with corresponding calculated uncertainties in dashed lines in the lower center, and the Nevzorov Probe total water content versus the OID and derived backscatter coefficients with corresponding trend lines in the lower right. . . . .	31
8	Plots showing results for the +5 °C case (15_08_01_14_37_31). The probe measured total concentrations versus time can be seen in the upper left, the cloud probes measured mean particle diameter versus time in the upper center, the calculated backscatter coefficient versus the particle diameter in the upper right, the cloud probes measured particle size spectrum (normalized by bin width and particle diameter) in the lower left, the Optical Ice Detector (OID) measured backscatter coefficients with the derived backscatter coefficients versus time on the y-axis with corresponding calculated uncertainties in dashed lines in the lower center, and the Nevzorov Probe total water content versus the OID and derived backscatter coefficients with corresponding trend lines in the lower right. . . . .	32
9	Plots showing results for the -35 °C case (15_07_31_18_18_35). The probe measured total concentrations versus time can be seen in the upper left, the cloud probes measured mean particle diameter versus time in the upper center, the calculated backscatter coefficient versus the particle diameter in the upper right, the cloud probes measured particle size spectrum (normalized by bin width and particle diameter) in the lower left, the Optical Ice Detector (OID) measured backscatter coefficients with the derived backscatter coefficients versus time on the y-axis with corresponding calculated uncertainties in dashed lines in the lower center, and the Nevzorov Probe total water content versus the OID and derived backscatter coefficients with corresponding trend lines in the lower right. . . . .	33

10	Plots showing results for the -45 °C case (15_08_01_18_20_11). The probe measured total concentrations versus time can be seen in the upper left, the cloud probes measured mean particle diameter versus time in the upper center, the calculated backscatter coefficient versus the particle diameter in the upper right, the cloud probes measured particle size spectrum (normalized by bin width and particle diameter) in the lower left, the Optical Ice Detector (OID) measured backscatter coefficients with the derived backscatter coefficients versus time on the y-axis with corresponding calculated uncertainties in dashed lines in the lower center, and the Nevzorov Probe total water content versus the OID and derived backscatter coefficients with corresponding trend lines in the lower right. . . . .	34
11	Plot showing the Nevzorov Probe total water content versus the Optical Ice Detector (OID) backscatter coefficients with a logarithmic x axis. The backscatter coefficients have been separated by water (black) and ice (blue) cases. . . . .	35
12	Plots showing the Nevzorov Probe total water content versus the derived backscatter coefficients with a logarithmic x axis. The backscatter coefficients have been separated by water (black) and ice (blue) cases. . . . .	36
13	Plots showing results for the +10 °C case (15_08_02_18_23_48) using data processed with the Reconstruction method. The probe measured total concentrations versus time can be seen in the upper left, the cloud probes measured mean particle diameter versus time in the upper center, the calculated backscatter coefficient versus the particle diameter in the upper right, the cloud probes measured particle size spectrum (normalized by bin width and particle diameter) in the lower left, the Optical Ice Detector (OID) measured backscatter coefficients with the derived backscatter coefficients versus time on the y-axis with corresponding calculated uncertainties in dashed lines in the lower center, and the Nevzorov Probe total water content versus the OID and derived backscatter coefficients with corresponding trend lines in the lower right. . . . .	39

14	Plots showing results for the +5 °C case (15_08_01_14_37_31) using data processed with the Reconstruction method. The probe measured total concentrations versus time can be seen in the upper left, the cloud probes measured mean particle diameter versus time in the upper center, the calculated backscatter coefficient versus the particle diameter in the upper right, the cloud probes measured particle size spectrum (normalized by bin width and particle diameter) in the lower left, the Optical Ice Detector (OID) measured backscatter coefficients with the derived backscatter coefficients versus time on the y-axis with corresponding calculated uncertainties in dashed lines in the lower center, and the Nevzorov Probe total water content versus the OID and derived backscatter coefficients with corresponding trend lines in the lower right. . . . .	40
15	Plots showing results for the -35 °C case (15_07_31_18_18_35) using data processed with the Reconstruction method. The probe measured total concentrations versus time can be seen in the upper left, the cloud probes measured mean particle diameter versus time in the upper center, the calculated backscatter coefficient versus the particle diameter in the upper right, the cloud probes measured particle size spectrum (normalized by bin width and particle diameter) in the lower left, the Optical Ice Detector (OID) measured backscatter coefficients with the derived backscatter coefficients versus time on the y-axis with corresponding calculated uncertainties in dashed lines in the lower center, and the Nevzorov Probe total water content versus the OID and derived backscatter coefficients with corresponding trend lines in the lower right. . . . .	41
16	Plots showing results for the -45 °C case (15_08_01_18_20_11) using data processed with the Reconstruction method. The probe measured total concentrations versus time can be seen in the upper left, the cloud probes measured mean particle diameter versus time in the upper center, the calculated backscatter coefficient versus the particle diameter in the upper right, the cloud probes measured particle size spectrum (normalized by bin width and particle diameter) in the lower left, the Optical Ice Detector (OID) measured backscatter coefficients with the derived backscatter coefficients versus time on the y-axis with corresponding calculated uncertainties in dashed lines in the lower center, and the Nevzorov Probe total water content versus the OID and derived backscatter coefficients with corresponding trend lines in the lower right. . . . .	42

## LIST OF TABLES

Table	Page
1	The list of channel numbers (Number) in the combined particle size distribution. Bin is the number of the channel from the different instruments, the Cloud Droplet Probe (CDP), 2 Dimensional Spectrometer (2D-S) and High Volume Precipitation Spectrometer Version 3 (HVPS3) probe. The Size Range gives the start and end size of the channel. Size Parameter gives the size parameter for the diameter range of the channel and a wavelength of 905 nm. Water gives the backscatter efficiencies used for the water cases and Ice gives the backscatter efficiencies used for the ice cases. 15

## ACKNOWLEDGMENTS

Thank you to David Delene, Mark Ray, and Andrew Detwiler, who reviewed the content and provided supplementing information and guidance. Optical Ice Detector data was provided by Kaare Anderson and Mark Ray at Collins Aerospace. Funding for this study was provided by the Department of Commerce. Thank you to NASA for providing the 2D-S, HVPS3, and Nevzorov Probe.

I dedicate this thesis to my always loving and supportive parents.

## ABSTRACT

A major aviation hazard is power loss caused by ice particle accumulation within jet engines. High-altitude cirrus clouds are especially dangerous since pilots are often unaware when the aircraft is flying in high ice particle conditions. The commercial aerospace industry is currently investigating several approaches to mitigate the risks posed by high-concentration ice crystal conditions. One such approach uses specially-designed airborne lidar systems to quantify high concentrations of ice crystals, which enables pilots, or engine control systems, to enact appropriate countermeasures. A key component in developing a high ice crystal concentration mitigation system is reference measurements of ice crystal size distributions taken by reliable cloud probes.

Research aircraft flights in Florida anvil cirrus clouds on 31 July 2015, 1 August 2015, and 2 August 2015 have segments with different temperatures, habits, and particle size distributions. Measurements with wing-mounted probes (Cloud Droplet Probe (CDP), Two-Dimensional Stereo (2D-S) probe, and High-Volume Precipitation Spectrometer Version Three (HVPS3)) are processed to obtain particle size distributions with a corresponding measurement uncertainty. The backscatter coefficient is calculated from *in-situ* measured particle size distribution using the backscatter efficiency determined using Mie theory. The comparison of the 1 Hz derived backscatter coefficient to the measured backscatter coefficient from an on-board lidar system known as the Optical Ice Detector (OID) shows varying degrees of agreement for the ice cases; however, there is a clear negative bias for the liquid water cases. Total water content measurements are correlated with changes in the OID Lidar measurements.

The agreement between the OID and cloud probe observations indicate that the OID could be used successfully to mitigate the ice particle risk for jet engines.



## CHAPTER 1

### INTRODUCTION

An important aircraft flight hazard is the ingestion of ice particles in the engines of high-altitude jets. A number of power loss events have occurred since 1990 which prompted revised regulations on acceptable flight conditions in cold clouds. Hence, aircraft need instruments capable of informing pilots when they are in dangerous environments. Internally mounted probes have been developed to detect high ice crystal environments. One such internally mounted probe, the Optical Icing Detector, is the focus of this study. The Background section provides information on the history surrounding the aircraft engine power loss hazard, as well as information regarding probes useful to the avoidance of ice crystal environments. The Aircraft Measurements section describes the North Dakota Citation II Research Aircraft, cloud probes, and instrumentation used to obtain the analyzed data set. Cloud probe measurements have uncertainties that are discussed through the proceeding sections. The Methodology section outlines processing of the aircraft probe data and the measurement uncertainty. The Results and Discussion section calculates backscatter coefficient values from 1 Hz cloud probe data and shows comparisons with lidar derived backscatter coefficients using case studies. Findings and their value to the scientific and aviation communities, are summarized in the Conclusions section. The overall goal is to compare Optical Ice Detector (OID) backscatter coefficients measurements with backscatter coefficients derived from state-of-the-art cloud probes and advanced image processing software. The scientific novelty is in determining the backscatter

coefficient uncertainty from uncertainties in the particle concentration and diameter uncertainty. The aircraft flight comparison that includes uncertainty assessment is a major step in the development of a lidar system to alert pilots of dangerous ice concentration conditions.

## CHAPTER 2

### BACKGROUND

#### 2.1 Ice Particle Icing

Since the early 1990s, there have been over 240 icing related incidents involving commuter and large transport aircraft at altitudes greater than 6,700 m above mean sea level (AMSL), which is the upper altitude limit at which the aviation industry considers supercooled liquid water to exist (Mason et al. 2006). Above 6,700 m AMSL, the atmosphere is cold enough to contain only ice particles with diameters from micrometers to centimeters. Ice particles are found above 6,700 m AMSL due to the freezing of liquid cloud droplets, particles falling from higher altitudes where homogeneous nucleation occurred, or ice particles colliding with supercooled liquid water to form rimed ice particles. Until the early 2000s, it was believed that ice particles were not a threat to aircraft performance since they would not adhere to the cold aircraft components. However, power loss incident frequency increased as long distance (and thus high altitude) flights increased. The analysis of forty-six aircraft power loss events with reliable environmental data indicated that the aircraft above 6,700 m AMSL would gradually lose power (Mason et al. 2006) and some engines experienced a total shut down. Once the aircraft descended to below 3,000 m AMSL, normal engine performance was restored, and failed engines were restarted. Research, analysis, and flight tests determined that the reduction in engine power was caused by ice buildup in the turbofan engine system (Mason et al. 2006).

Aircraft power loss incidents consistently occurred near convective clouds, which lead to the idea that rain or hail was quickly lifted to high altitudes by updrafts that affected the engines. While the pilot reports mentioned being in a cloud, no reference was made to air frame icing or any other remarkable weather encounter. Investigative efforts were hindered by the lack of data on the older transport aircraft; however, the limited information available indicated that there was no high radar reflectivity or turbulence at the event location. Furthermore, no damage to the air frame by hail was found. Finding no signs of heavy precipitation or external physical damage to the plane, investigators could not determine the cause of the power loss. Airflow through the engines was thought to be too quick for sufficient heat transfer from the engine surfaces to ice crystals for partial melting and refreezing onto engine surfaces (Mason et al. 2006). Furthermore, if airflow was not fast enough to prevent melting and refreezing, it was assumed that temperatures within the engine would be sufficient to completely melt the particles and prevent refreezing on contact with the metal surface. Despite no concrete evidence for the power loss, it was decided to raise the descent rotor speeds of the transport aircraft engines to hopefully reduce the occurrence of engine power loss. Increasing rotor speeds during descent increased the engine rotor temperatures and reduced the problem for some transport engines.

With the power loss issue addressed and seemingly improved, little was done to further explore the cause, and the reason for the engine power loss remained an unsolved issue until a 2002 event where a transport aircraft with dual ice detectors experienced engine power loss without the presence of supercooled liquid water (Mason et al. 2006). Analysis of the 2002 event lead to the understanding that ice accretion can take place in environments consisting entirely of ice crystals, not just in environments with supercooled liquid water. In 2003, the Federal Aviation Administration (FAA) Ice Protection Harmonization Working Group met to discuss flight

protocols in high ice concentration conditions. At the FAA meeting, the similarities between commuter and transport power loss scenarios were fully realized, and it was concluded that clouds did not need super-cooled liquid water to significantly affect engine performance. The hazard to aircraft due to ice particles causing engine power loss is termed “ice particle icing” (Mason et al. 2006) to differentiate it from “icing” of surfaces from the impaction of super-cooled liquid cloud droplets. Ice particle icing caused permanent damage to the engine compressors during a 2013 event that occurred above 10 km. The 2013 event prompted the issuance of Airworthiness Directive 2013-NM-209-AD on 27 November 2013. Airworthiness Directives are legally enforceable regulations issued by the FAA in accordance with 14 CFR part 39 to correct an unsafe condition in a product or situation. 2013-NM-209-AD required specific Boeing aircraft (models 747-8, 747-8f, and 787-8) to advise the attending flight crew of potential ice particle icing conditions and to update procedures to prohibit any operation in high ice concentrations. As per the directive, operations at or above 9,100 m AMSL must include the flight crew complying with the FAA’s Avoidance of Ice Crystal Icing Procedure. Since cirrus clouds are often not visible to pilots, they can be a particularly large risk for high altitude, long duration flight operations of high-performance jet engines. Mitigating engine power loss due to the ice particle icing risk requires instruments to measure the ice particle concentrations so pilots can be alerted to potentially dangerous environments.

## 2.2 Cloud Probes

Research grade instruments for ice concentration and size have been available since the 1970s. Optical array probes are common research instruments that measure the two-dimensional size and concentration of cloud particles (see Figure 1). To avoid major external air-frame modifications, companies have developed instruments mounted

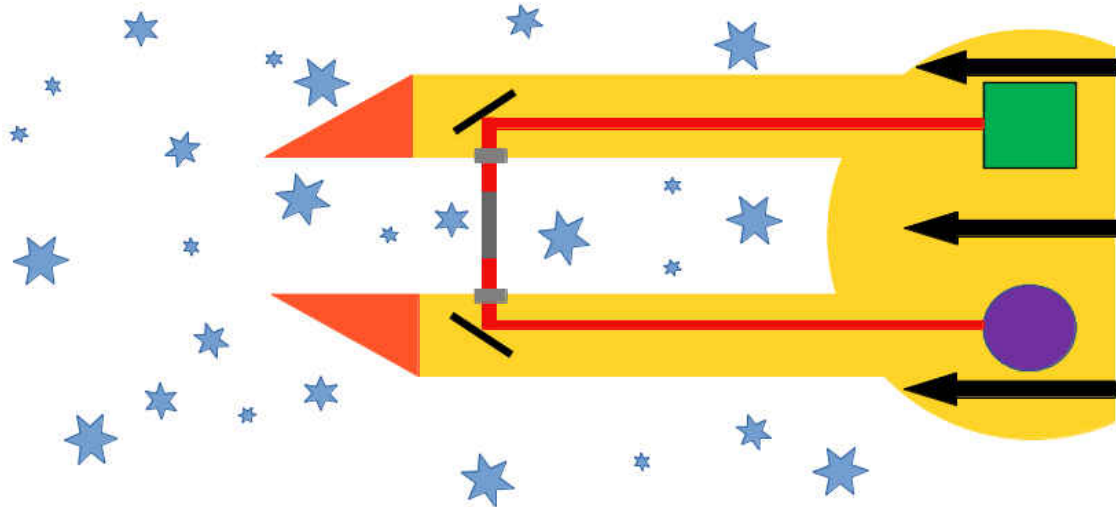


Figure 1: Side view illustration showing the general features of an optical array probe, which images cloud particles as the probe moves forward (black arrows) through the air. Ice crystals (indicated in blue) encounter the laser beam (red lines) which passes through the optical windows (light gray boxes) and block the light emitted by the laser beam generator (green box). Heated, anti-shattering tips (orange triangles) prevent ice build up and reduce broken particles falling into the depth of field (dark gray rectangle). Images are recorded of the photodiode array elements (purple oval) when at least one element is reduced in intensity by 50 %. The sampling of the array elements is synchronized to the air speed of the probe to create a two-dimensional image.

internally that do not affect the aircraft lift. One such system is the Backscatter Cloud Probe (BCP) (Beswick et al. 2014) which uses an internally mounted laser system to measure cloud droplet concentration without altering the airflow around the aircraft. The BCP was shown to be able to accurately measure particle size distributions from a commercial aircraft platform (Beswick et al. 2015). Another internally mounted instrument is the Optical Ice Detector (OID) (Ray et al. 2009; Halama et al. 2010; Ray and Anderson 2015). There are two main differences between the OID and BCP. The BCP observes a small ( $125 \text{ cm}^3$  at  $100 \text{ m s}^{-1}$  sample volume approximately 4 cm away from the aircraft (Beswick et al. 2014), while the OID observes a conical volume ( $4,500 \text{ cm}^3$ ) extending up to 10 m from the airplane (Ray and Anderson 2015). The BCP has a single orientation, linearly polarized wavelength of 658 nm, while the OID has a randomly orientated, linearly polarized wavelength of 1550 nm and a circularly polarized wavelength of 905 nm. Circular polarization provides discrimination between water and ice particles by relating the depolarization of the backscattered light to the initial polarization of the probe emitted beam. The properties of electromagnetic waves are often represented using a four-component matrix comprised of the Stokes parameters (Liou and Yang 2016). The components consist of I (total intensity), Q (horizontal vs. vertical polarization), U ( $45^\circ$  polarization), and V (circular polarization) (Hulst 1981). When circularly polarized light scatters backward from a liquid water droplet, the rotational sense of the polarization remains the same due to the smooth surface of spherical droplets but the direction of the propagation is reversed, thus reversing the sign of the polarization (component V, also known as the fourth Stokes parameter) with respect to the transmitted probe laser. For example, if the transmitted laser beam has a fourth Stokes parameter  $V = 1$ , the Stokes parameter for backscatter from water droplets is ideally -1. In reality, multiple scattering within a dense water cloud creates some depolarization that depends on the

density. When circularly polarized laser light scatters backward from ice crystals, the polarization purity is degraded due to internal reflections from the crystal facets. The direction of propagation is reversed for ice; however, the degree of polarization caused by the ice crystals results in the sign of the fourth Stokes to be near zero or positive. The fourth Stokes parameter allows a cloud to be determined to be composed entirely of ice (a fourth Stokes parameter approximately zero or slightly positive), entirely of water (a fourth Stokes parameter nearly -1), or of both ice and water (a fourth Stokes parameter between 0 and -1, with the value depending on the optical density of the cloud). Furthermore, computing a ratio of the amount of backscatter at the 905 nm wavelength to the backscatter at the 1550 nm wavelength (known as two-color lidar (Westbrook et al. 2010)) provides a method for determining the effective droplet diameter. Backscatter from the 1550 nm wavelength of the OID is not considered in this study. The OID samples at a rate of five samples per second. These samples are averaged to produce a 1 Hz data set used for this study.



## CHAPTER 3

### AIRCRAFT MEASUREMENTS

The North Dakota Citation II Research Aircraft is a jet manufactured by Cessna and modified for conducting atmospheric research (Delene et al. 2019). The aircraft instruments measure aircraft speed and position, along with atmospheric state parameters such as temperature, relative humidity, and winds. The North Dakota Citation II Research Aircraft has conducted multiple field projects in a variety of locations focusing on cloud microphysical observations (Skofronick-Jackson et al. 2014; Jensen et al. 2015; Schmidt et al. 2019). Typically, each field project uses a different suite of instruments. There are several data sets available for analysis; however, this study only uses 2015 Florida field project (CAPE2015) flights. While other projects included OID measurements, CAPE2015 included measurements of high altitude, cirrus clouds in the anvils of convective storms. The CAPE2015 aircraft instrumentation (Figure 2) includes the 2-Dimensional Stereo (2D-S) probe (Lawson et al. 2006), the Cloud Droplet Probe (CDP) (Lance et al. 2010), the High-Volume Precipitation Spectrometer Version 3 (HVPS3) probe (Kumjian et al. 2016), and the Nevzorov Probe (Korolev et al. 2013a). The OID is mounted inside the Citation Research Aircraft, viewing through an optical window that allows light emitted from the OID to sample a horizontal column of the air-stream stretching the full span of the wing (see Figure 2). The Nevzorov probe is a constant-temperature, hot-wire probe used to measure the liquid and total water content of clouds (Korolev et al. 1998). Two sensors are included on the probe. A total water content sensor consists of a conical

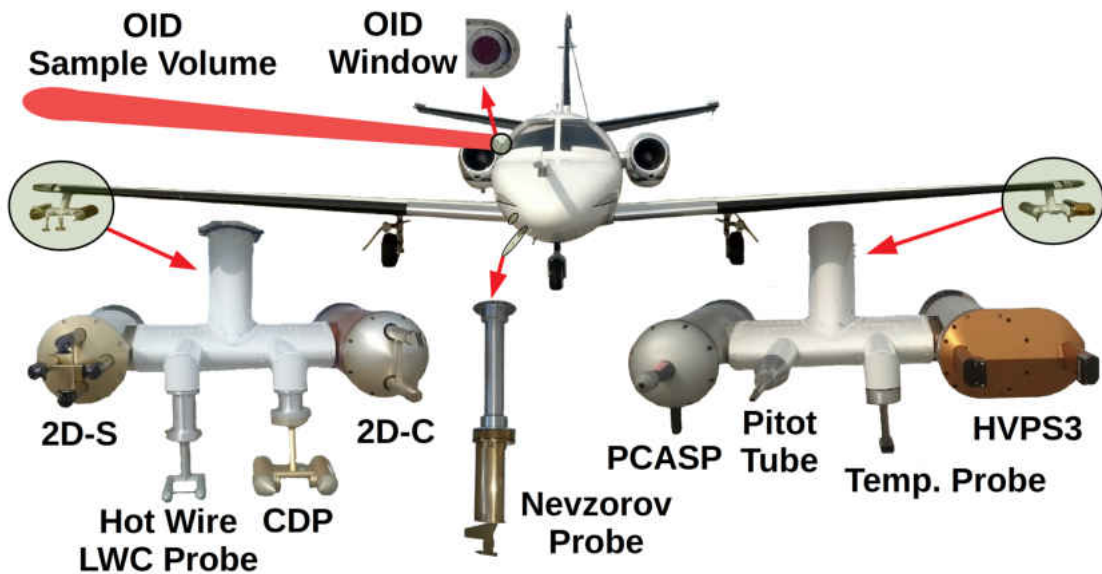


Figure 2: Image showing the North Dakota Citation II Research Aircraft and instrumented pylons as configured for the Florida 2015 campaign. The optical window used by the Optical Ice Detector (OID) is shown in the upper left, which is angled slightly so the sampling region is in front of, and level with, the wing (labeled “OID Sample Volume”). The Cloud Droplet Probe (CDP) is used for measuring cloud droplets with the smallest of the diameters. The 2 Dimensional Cloud probe (2D-C) uses a 32-photodiode array of  $30\ \mu\text{m}$  elements. The 2 Dimensional Stereo (2D-S) probe uses two linear 128 photodiode arrays and the High Volume Precipitation Spectrometer Version 3 (HVPS3) a single linear 128-photodiode array to sample particles in the mid-size diameter range and the large diameter range, respectively. The Nevzorov Probe is a hot-wire probe used to measure the liquid water content, ice water content, and total water content.

receiver which collects both liquid water droplets and ice crystals. A liquid water content sensor uses a flat plate with an exposed edge for water droplet collection. Both sensors have corresponding reference wires which are exposed to the same airflow but do not interact with cloud particles. The temperature difference between the collection sensors and their reference wires is converted into liquid water and total water contents using heat transfer equations. Ice water content is calculated by subtracting the liquid water content from the total water content.

### 3.1 Ice Particle Formation

Determining the conditions which form specific ice crystal habits has challenged researchers since the 1940s (Bailey and Hallett 2009). Forward scattering probes such as the CDP do not discriminate between water and ice particles. Optical array probes such as the 2D-S and HVPS3, rarely provide the image detail required to discriminate between the smallest features of the image, rendering automatic habit classification difficult. Cloud imaging probes use charge-coupled device (CCD) cameras to obtain high resolution images of ice particles. A well-known example is the Cloud Particle Imager (CPI) (Lawson et al. 2001), which uses a 1 Megapixel CCD camera triggered by a 25 ns pulsed, coherent laser diode. The CPI images are processed to measure particle size, shape, concentration, and most importantly, particle habit. Bailey and Hallett 2009 use CPI data collected in various works [e.g. (Korolev et al. 1999)] to produce a comprehensive habit diagram based on temperature and ice supersaturation. Bailey and Hallett determined that at temperatures from  $-20\text{ }^{\circ}\text{C}$  to  $-40\text{ }^{\circ}\text{C}$  plate-like habits are most common, columnar shapes dominate in the  $-40\text{ }^{\circ}\text{C}$  to  $-60\text{ }^{\circ}\text{C}$  range, and needles are most prevalent from  $-60\text{ }^{\circ}\text{C}$  and colder. Ice supersaturation plays a smaller role than temperature in the formation of particle habits. Supersaturation occurs when there is more water vapor available than is thermodynamically required

to form the condensed phase of water (Yau and Rogers, 1989). Due to the abundance of hygroscopic aerosols (suspended particles in the atmosphere), supersaturations in clouds rarely reach above 1 %. Ice supersaturations below 0.2 % tend to shift habits into a more plate like regime at all temperatures. While these temperature guidelines apply to the habit where ice forms, how the particles continue to grow depends on their environment after formation. Once formed, particles can be moved to an environment of different temperatures and supersaturations due to falling, convection, and advection. A probe similar to the CPI, known as the Particle Habit Imaging and Polar Scattering (PHIPS) probe (Schön et al. 2011) uses two CCD cameras to take two simultaneous, stereographic photos of individual particles. Unlike the CPI, which uses a beam of coherent infrared pulses to image encountered particles, the PHIPS uses an incoherent visible light (690 nm wavelength) to illuminate particles as they pass through the depth of field of the cameras. The result is that the PHIPS has clearer images than the CPI due to the lack of diffraction normally caused by coherent light. The PHIPS also incorporates a polar nephelometer which provides radiation scattering properties of sampled particles through twenty light collecting channels at an angular range of  $18^\circ$  to  $170^\circ$  (Schnaiter et al. 2018). The CapeEx19 field project (Summer of 2019) in Florida deployed the PHIPS to provide valuable particle backscattering and habit information; however, the CAPE2015 field project only had the 2D-S for image identification of particle habit.

## CHAPTER 4

### METHODOLOGY

#### 4.1 Data Processing

Quality assurance of the cloud probe data involves systematic review by instrumentation experts to ensure the data are satisfactory to use for the intended scientific analysis. Quality checks entail procedures for visually assessing image quality and determining if any of the instrument diodes are malfunctioning by evaluating base-state voltages. Data quality assurance and processing are conducted using the open source Airborne Data Processing and Analysis Software Package (ADPAA) (Delene 2011). Processing of particle images to obtain a size distribution is done using the System for Optical Array Probe Data Analysis Version 2 (SODA2) (Bansemer 2013) software package. An entire field project is automatically processed at once using linked SODA scripts provided in ADPAA. A work-flow script is used to document the configuration and all processing used for the project analysis (OID Analysis 2019). The fast-circle, or circle-fit, method is used to determine particle diameter by enclosing the image with the smallest circle that fully encompasses the entirety of the particle (Wu and McFarquhar 2016). The diameter of the enclosing circle is used as the particle diameter. A correction is also applied to the processing of data containing water droplets following the methods of (Korolev 2007). The diffraction of light by spherical liquid water droplets can result in the particle image appearing larger with a bright spot in the center. The central bright spot is known as a Poisson spot. SODA2 corrects for Poisson spots by comparing the detected area of the spot to the whole image and

generating a correction factor. The correction factor is used to reduce the particle size to the expected value. The All-In method (Heymsfield and Parrish 1978) is used to process two-dimensional images obtained by the 2D-S and HVPS3 probes. All-In processing entails using only optical array probe images where the particle is entirely within the photo-diode array. Determining the full particle size from a partially imaged particle (i.e. only part of the particle is within the photo-diode array) introduces uncertainty for irregularly shaped particles but is possible using the Reconstruction method. The Reconstruction method uses particle images that are partially captured within the imaging diode array. The part of the particle outside the image diode array are assumed to be symmetrical with the particle within the diode array and the missing portion of the particle is recreated to increase the particle size measurement. HVPS3 measurements are available; therefore, the particle size range is completely covered by the three probes and Reconstruction is not necessary. The optical array probe particle size distributions used herein only use the All-In method; however, the Reconstruction method has also been used to create a combined particle size distribution (Appendix A). The ADPAA script `merge_cdp_2ds_hvps3.py` combines CDP (2-5  $\mu\text{m}$ ), 2D-S (45-1,000  $\mu\text{m}$ ), and HVPS3 (1,000-30,000  $\mu\text{m}$ ) measurements to create one particle size distribution for analysis (Table 1). The total number concentration and mean particle diameter are derived from the combined spectrum using all particle sizes. The smallest measured particles (less than 100  $\mu\text{m}$  diameter) are frequently the result of larger particles shattering on contact with the probe tips and can often be considered erroneous to the data set (Korolev et al. 2013b; Korolev and Isaac 2005). Korolev anti-shatter tips are used on the probe heads to reduce the number of tip-generated small particles. Following the methods of (Field et al. 2006) SODA2 uses inter-arrival times of encountered particles as a rejection criterion. If a particle

is sampled within 0.2 ms of the preceding sampled particle, the former is rejected as a shattering artifact.

Table 1: The list of channel numbers (Number) in the combined particle size distribution. Bin is the number of the channel from the different instruments, the Cloud Droplet Probe (CDP), 2 Dimensional Spectrometer (2D-S) and High Volume Precipitation Spectrometer Version 3 (HVPS3) probe. The Size Range gives the start and end size of the channel. Size Parameter gives the size parameter for the diameter range of the channel and a wavelength of 905 nm. Water gives the backscatter efficiencies used for the water cases and Ice gives the backscatter efficiencies used for the ice cases.

Number	Probe	Bin	Size Range	Size Parameter	Water	Ice
1	CDP	1/30	2-3 $\mu\text{m}$	7 - 10	0.190	0.150
2	CDP	2/30	3-4 $\mu\text{m}$	10 - 14	1.367	1.095
3	CDP	3/30	4-5 $\mu\text{m}$	14 - 17	2.480	1.647
4	CDP	4/30	5-6 $\mu\text{m}$	17 - 21	1.968	1.782
5	CDP	5/30	6-7 $\mu\text{m}$	21 - 24	1.860	2.652
6	CDP	6/30	7-8 $\mu\text{m}$	24 - 27	1.413	1.741
7	CDP	7/30	8-9 $\mu\text{m}$	27 - 31	0.859	0.930
8	CDP	8/30	9-10 $\mu\text{m}$	31 - 35	0.650	0.849
9	CDP	9/30	10-11 $\mu\text{m}$	35 - 38	1.529	1.246
10	CDP	10/30	11-12 $\mu\text{m}$	38 - 42	2.137	1.170
11	CDP	11/30	12-13 $\mu\text{m}$	42 - 45	1.537	1.199
12	CDP	12/30	13-14 $\mu\text{m}$	45 - 49	1.110	1.871
13	CDP	13/30	14-16 $\mu\text{m}$	49 - 56	1.326	1.668
14	CDP	14/30	16-18 $\mu\text{m}$	56 - 62	1.203	1.419
15	CDP	15/30	18-20 $\mu\text{m}$	62 - 69	1.891	1.544
16	CDP	16/30	20-22 $\mu\text{m}$	69 - 76	0.974	1.801
17	CDP	17/30	22-24 $\mu\text{m}$	76 - 83	1.648	1.401

18	CDP	18/30	24-26 $\mu\text{m}$	83 - 90	1.340	1.700
19	CDP	19/30	26-28 $\mu\text{m}$	90 - 97	1.525	1.890
20	CDP	20/30	28-30 $\mu\text{m}$	97 - 104	1.148	1.800
21	CDP	21/30	30-32 $\mu\text{m}$	104 - 111	1.827	1.555
22	CDP	22/30	32-34 $\mu\text{m}$	111 - 118	1.152	1.859
23	CDP	23/30	34-36 $\mu\text{m}$	118 - 125	1.515	2.172
24	CDP	24/30	36-38 $\mu\text{m}$	125 - 132	1.370	1.618
25	CDP	25/30	38-40 $\mu\text{m}$	132 - 139	1.522	1.799
26	CDP	26/30	40-42 $\mu\text{m}$	139 - 146	1.166	1.802
27	CDP	27/30	42-44 $\mu\text{m}$	146 - 153	1.697	2.009
28	CDP	28/30	44-45 $\mu\text{m}$	153 - 156	1.142	1.611
29	2D-S	5/29	45-55 $\mu\text{m}$	156 - 191	1.597	1.874
30	2D-S	6/29	55-65 $\mu\text{m}$	191 - 226	1.404	1.772
31	2D-S	7/29	65-75 $\mu\text{m}$	226 - 260	1.599	1.637
32	2D-S	8/29	75-85 $\mu\text{m}$	260 - 295	1.524	1.682
33	2D-S	9/29	85-95 $\mu\text{m}$	295 - 330	1.650	1.598
34	2D-S	10/29	95-105 $\mu\text{m}$	330 - 364	1.740	1.773
35	2D-S	11/29	105-125 $\mu\text{m}$	364 - 434	1.856	1.460
36	2D-S	12/29	125-145 $\mu\text{m}$	434 - 503	2.076	1.266
37	2D-S	13/29	145-175 $\mu\text{m}$	503 - 607	2.246	1.183
38	2D-S	14/29	175-225 $\mu\text{m}$	607 - 781	2.586	1.003
39	2D-S	15/29	225-275 $\mu\text{m}$	781 - 955	3.108	0.935
40	2D-S	16/29	275-325 $\mu\text{m}$	955 - 1,128	3.284	0.766
41	2D-S	17/29	325-400 $\mu\text{m}$	1,128 - 1,389	3.758	0.880
42	2D-S	18/29	400-475 $\mu\text{m}$	1,389 - 1,649	4.005	0.653
43	2D-S	19/29	475-550 $\mu\text{m}$	1,649 - 1,909	4.532	0.948



44	2D-S	20/29	550-625 $\mu\text{m}$	1,909 - 2,170	4.395	0.692
45	2D-S	21/29	625-700 $\mu\text{m}$	2,170 - 2,430	4.904	1.206
46	2D-S	22/29	700-800 $\mu\text{m}$	2,430 - 2,777	5.015	0.565
47	2D-S	23/29	800-900 $\mu\text{m}$	2,777 - 3,124	5.481	1.168
48	2D-S	24/29	900-1,000 $\mu\text{m}$	3,124 - 3,471	6.188	0.567
49	HVPS3	5/28	1,000-1,200 $\mu\text{m}$	3,471 - 4,166	6.477	0.918
50	HVPS3	6/28	1,200-1,400 $\mu\text{m}$	4,166 - 4,860	7.263	0.724
51	HVPS3	7/28	1,400-1,600 $\mu\text{m}$	4,860 - 5,554	7.677	0.722
52	HVPS3	8/28	1,600-1,800 $\mu\text{m}$	5,554 - 6,248	8.772	0.798
53	HVPS3	9/28	1,800-2,200 $\mu\text{m}$	6,248 - 7,637	9.380	1.214
54	HVPS3	10/28	2,200-2,600 $\mu\text{m}$	7,637 - 9,025	11.13	0.825
55	HVPS3	11/28	2,600-3,000 $\mu\text{m}$	9,025 - 10,414	12.35	0.978
56	HVPS3	12/28	3,000-3,400 $\mu\text{m}$	10,414 - 11,803	14.16	1.075
57	HVPS3	13/28	3,400-3,800 $\mu\text{m}$	11,803 - 13,191	16.93	9.402
58	HVPS3	14/28	3,800-4,200 $\mu\text{m}$	13,191 - 14,580	18.47	1.914
59	HVPS3	15/28	4,200-4,600 $\mu\text{m}$	14,580 - 15,968	28.51	1.524
60	HVPS3	16/28	4,600-5,000 $\mu\text{m}$	15,968 - 17,357	19.80	3.278
61	HVPS3	17/28	5,000-6,000 $\mu\text{m}$	17,357 - 20,828	22.42	2.885
62	HVPS3	18/28	6,000-7,000 $\mu\text{m}$	20,828 - 24,300	22.14	7.140
63	HVPS3	19/28	7,000-8,000 $\mu\text{m}$	24,300 - 27,771	78.76	4.648
64	HVPS3	20/28	8,000-9,000 $\mu\text{m}$	27,771 - 31,242	27.61	10.71
65	HVPS3	21/28	9,000-10,000 $\mu\text{m}$	31,242 - 34,714	33.42	7.602
66	HVPS3	22/28	10,000-12,000 $\mu\text{m}$	34,714 - 41,656	45.03	24.69
67	HVPS3	23/28	12,000-14,000 $\mu\text{m}$	41,656 - 48,599	37.24	37.16
68	HVPS3	24/28	14,000-16,000 $\mu\text{m}$	48,599 - 55,542	61.52	26.18
69	HVPS3	25/28	16,000-18,000 $\mu\text{m}$	55,542 - 62,485	939.6	27.34

70	HVPS3	26/28	18,000-20,000 $\mu\text{m}$	62,485 - 69,427	163.2	80.80
71	HVPS3	27/28	20,000-25,000 $\mu\text{m}$	69,427 - 86,784	154.9	108.1
72	HVPS3	28/28	25,000-30,000 $\mu\text{m}$	86,784 - 104,141	827.6	80.53

## 4.2 Probe Equations

Calculation of an optical array probe sample volume is done using

$$SV = SA * TAS * t, \quad (4.1)$$

where  $SV$  is the sample volume (in  $\text{m}^3$ ),  $SA$  is the sample area (in  $\text{m}^2$ ),  $TAS$  is the true airspeed of the aircraft (in  $\text{m s}^{-1}$ ), and  $t$  is the elapsed time (in s) (McFarquhar et al. 2017). The  $TAS$  is provided by aircraft pitot tube measurements (Figure 2) and  $SA$  is determined using

$$SA = DOF * w, \quad (4.2)$$

where  $DOF$  is the depth of field (in m) and  $w$  is the effective width of the photodiode array (in m). The  $DOF$  is the region along the laser beam where particles are sufficiently within focus to be sized accurately. Optical array probes, such as the 2D-S and HVPS3, require photodiodes to have at least 50 % of their light blocked before the diode is considered “shadowed”. If less than 50 % of light is blocked, the diodes are not “shadowed” and no image is taken. Out of focus particles (particles outside the  $DOF$ ) often do not produce strong enough shadows to be detected and are thus frequently ignored (Korolev 2007).

### 4.3 Light Scattering

Scattering probes, such as the Cloud Droplet Probe (CDP) (Lance et al. 2010), use forward scattering intensity to determine particle size. The CDP has an open path laser beam (658 nm) between two arms so particles that enter the beam scatter light into the forward direction at a range of 4 ° to 12 °, and is detected by a photodiode. The measured intensity is converted into a particle size using Mie scattering theory. The CDP sampling area is set within ADPAA processing scripts at 0.24 mm<sup>2</sup>, as recommended by the manufacturer. However, work has suggested that the manufacturer value can be too low, causing the CDP measured concentrations to be too high (Faber et al. 2018). Particles larger than 50 μm in diameter are not sized by the CDP due to the small sample area resulting in a low number of counts.

There are three primary light-scattering regimes which exist for particles in the atmosphere: geometric, Mie, and Rayleigh scattering. Which scattering regime applies depends on the particle-diameter to incident-light-wavelength ratio calculated using

$$\alpha = \frac{\pi D}{\lambda}, \quad (4.3)$$

where  $\alpha$  is the size parameter (unitless),  $D$  is the cloud particle diameter (in m), and  $\lambda$  is the wavelength of incident light (in m) (Hulst 1981). When  $\alpha$  is equal to or greater than 100 the geometric scattering regime applies, when  $\alpha$  is between 0.1 and 100 the Mie scattering regime applies, and when  $\alpha$  is equal to or less than 0.1 the Rayleigh scattering regime applies (Bohren and Huffman 1983). For this study,  $\lambda$  is fixed at 905 nm (for the purposes of this study the 1550 nm wavelength of the OID is excluded) allowing for classification of the scattering regime based only on the changing particle diameter. Thus, particles equal to or larger than approximately 30 μm in diameter are in the geometric regime, particles between 0.03 μm and 30 μm in diameter are in

the Mie regime, and particles with diameters equal to or less than 0.03  $\mu\text{m}$  are in the Rayleigh regime (Table 1). Table 1 shows that most channels contain particles larger than 30  $\mu\text{m}$  and therefore the geometric scattering regime applies. However, since calculations performed for the geometric regime are expanded versions of the Mie calculations, code used for particles less than 30  $\mu\text{m}$  is applied to the larger particles as well.

OID measurements of extinction coefficients and backscatter coefficients assume a homogeneous cloud particle distribution over the sampling distance and are determined by inverting the equation for the returned lidar power  $P(r)$  [see (Ray and Anderson 2015)]

$$P_R = \beta G_R e^{-2\alpha R}, \quad (4.4)$$

where  $\beta$  is the backscatter coefficient (in  $\text{m}^{-1} \text{sr}^{-1}$ ),  $G_R$  is a light collection efficiency as a function of particle range,  $\alpha$  is the extinction coefficient (in  $\text{m}^{-1}$ ), and  $R$  is the range of the particles (in  $\text{m}$ ) from the OID.  $\beta$  depends on the number concentration, the particle diameter, and the particle scattering efficiency at  $180^\circ$  (backscatter efficiency) (Bohren and Huffman 1983). The backscatter coefficient can thus be calculated using (Zhang et al. 2015)

$$\beta_{ECP} = \sum_{i=1}^{i=\max} \frac{\eta_i Q_i \pi r_i^2}{4\pi}, \quad (4.5)$$

where  $\beta_{ECP}$  is the microphysically derived backscatter from the external cloud probes (in  $\text{m}^{-1} \text{sr}^{-1}$ ),  $i$  is the particle channel number of the combined distribution (Table 1),  $\eta_i$  is the number of particles in the channel (in  $\text{m}^{-3}$ ),  $Q_i$  is the scattering efficiency at  $180^\circ$  by channel (unitless), and  $r_i$  is the particle radius of the channel midpoint (in  $\text{m}$ ). The number concentration and particle radius are from the combined particle spectrum (Table 1). The denominator of  $4\pi$  is used as a steradian normalization

factor to account for the OID receiving backscattered radiation in terms of a point source rather than from an entire subtended sphere (Jaffey 1954).

The phase function is a measure of how much light is scattered by a particle in different directions (Hulst 1981) and largely depends on the shape and roughness of the particle, which is determined by the habit. The scattering efficiency is a function of scattering angle and is provided by a readily available python module called “miepython” (Prah1 2019). “Miepython” provides the scattering efficiency given the particle diameter and the refractive index of an incident wavelength (e.g. 905 nm). Following (Kedenburg et al. 2012) the refractive index of water is set to  $1.3263 + 5.61 \times 10^{-7}j$ , where 1.3263 is the real component and  $5.61 \times 10^{-7}j$  is an imaginary component which accounts for absorption. The refractive index of ice is set to  $1.3031 + 5.61 \times 10^{-7}j$  (Warren and Brandt 2008). Efficiencies are calculated for 100 equally spaced points within each probe channel size range. These values are then averaged to be used with each probe channel midpoint during calculation of the backscatter coefficients. Values for the backscatter efficiency of water and ice can be seen in Table 1.

Backscatter (1 Hz) from the OID and the cloud probe suite (using Eq 4.5) are compared for agreement in terms of absolute magnitude and relative changes. To judge the agreement between the compared backscatter it is important to quantify the uncertainty in each parameter. The uncertainty equation for the derived backscatter for a single channel number (i) is obtained following the method for the product of two variables on page 44 of (Baird 1988) by taking the partial derivative of Eq. 4.5 with respect to the particle concentration and particle radius, and given by

$$\delta\beta_{ECPi} = \frac{Q_i\pi r_i^2}{4\pi}\delta\eta_i + \frac{\eta_i Q_i\pi r_i}{2\pi}\delta r_i, \quad (4.6)$$

where  $\delta\beta_{ECP_i}$  is the uncertainty of  $\beta_{ECP_i}$  (in  $\text{m}^{-1} \text{sr}^{-1}$ ),  $\delta\eta_i$  is the uncertainty in the measured concentration (in  $\text{m}^{-3}$ ), and  $\delta r_i$  is the uncertainty in the measured particle radius (in m).  $\delta\eta_i$  is calculated using a least squares method (Horvath et al. 1990)

$$\delta\eta_i = \frac{\eta_i}{\sqrt{\text{countedparticles}}}, \quad (4.7)$$

and  $\delta r_i$  is taken to be the half width of channel  $r_i$ . Using the channel half width is a lower bound on the uncertainty, which could be larger due to small particles being outside the depth of field (O'Shea et al. 2019) and non-spherical large particles. The total, or overall, uncertainty is the sum of the backscatter uncertainty of all the channels. Uncertainty in the OID data is generated by calculating the standard deviation of the five measurements which were averaged to produce the 1 Hz data set.

## CHAPTER 5

### DATA SET

Case study analysis is performed using data taken during the 2015 CAPE campaign over Florida. Ice particle icing usually occurs at altitudes of 8,000 m AMSL or greater since temperatures well below 0 °C are necessary for the event to occur. Thus, cases for analysis are selected based on their altitude, temperature, and relative constancy of the cloud data. Four cases from the CAPE2015 field project are chosen which have consistent temperatures: `flight 15_07_31_18_18_35` (henceforth referred to as -35 °C case), `flight 15_08_01_14_37_31` (+5 °C case), `flight 15_08_01_18_20_11` (-45 °C case), and `flight 15_08_02_18_23_48` (+10 °C case). As seen in Figure 3, the +10 °C case is at an altitude of 3 km GPS with a temperature of 10 °C. The associated 2D-S images include very small spherical particles indicating water droplets. Shown in Figure 4 is the +5 °C case which was at an altitude of 3.5 km and temperature just below 5 °C. The 2D-S images show small, spherical particles, again confirming the presence of liquid water. Figure 5 shows the altitude, temperature, and 2D-S imaged particles from the -35 °C case. An altitude of 9.5 km is maintained with a temperature of -35 °C for the span of the analyzed data. The 2D-S images show irregularly shaped particles, further confirming the environment contains ice crystals. Figure 6 shows -45 °C case at an altitude of 11 km, with a temperature of -45 °C during the analyzed time. 2D-S images again show irregularly shaped particles, confirming the presence of ice crystals.

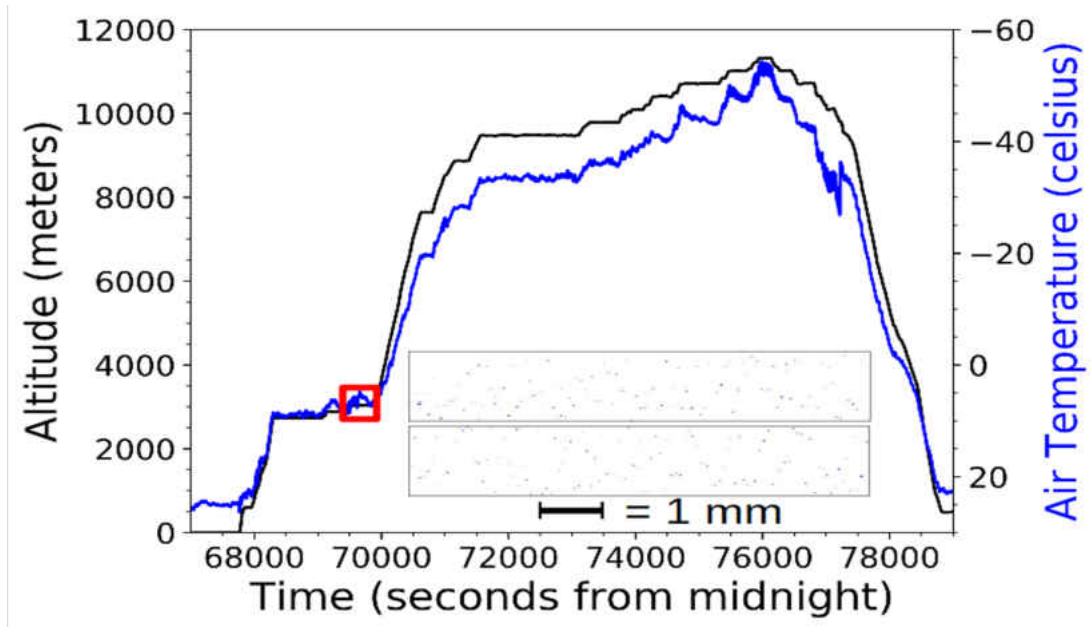


Figure 3: Plot showing the altitude (black) and air temperature (blue) sampled during the North Dakota Citation II Research Aircraft’s flight on 02 August 2015 (+10 °C case). Measurements focused on high altitude anvil cirrus clouds produced by intense convection. The red rectangle indicates the time segment (69,510 – 69,570 s from midnight UTC) analyzed, where the average altitude is 3,400 m GPS and the average temperature is 10 °C. The center panels contain 2D-S images from the analyzed time.



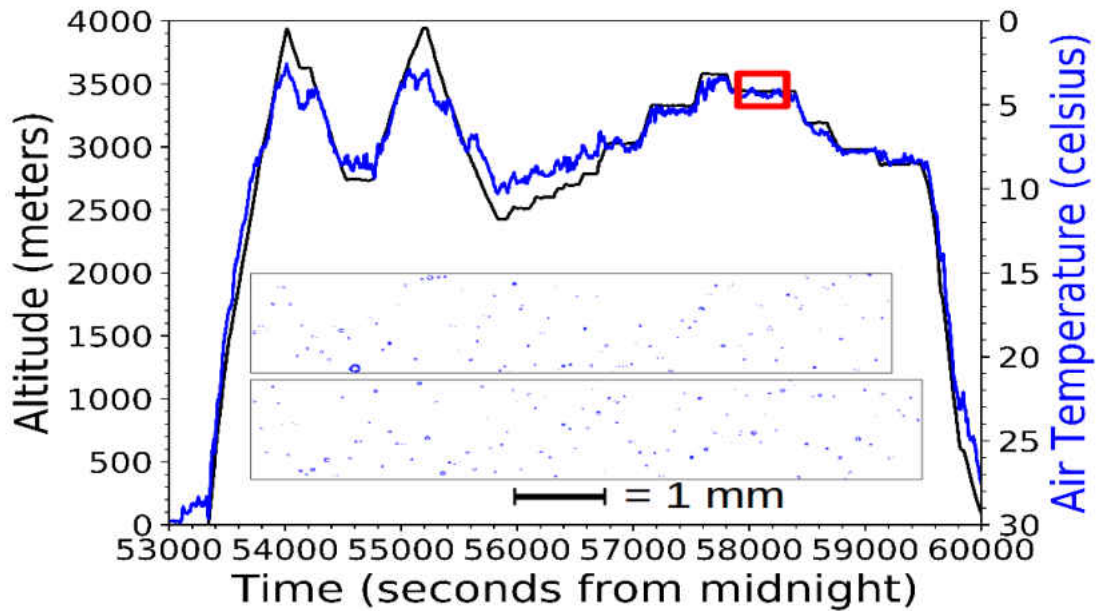


Figure 4: Plot showing the altitude (black) and air temperature (blue) sampled during the North Dakota Citation II Research Aircraft's flight on 01 August 2015 (+5 °C case). Measurements focused on high altitude anvil cirrus clouds produced by intense convection. The red rectangle indicates the time segment (57,850 – 57,910 s from midnight UTC) analyzed, where the average altitude is 3,400 m GPS and the average temperature is 5 °C. The center panels contain 2D-S images from the analyzed time.

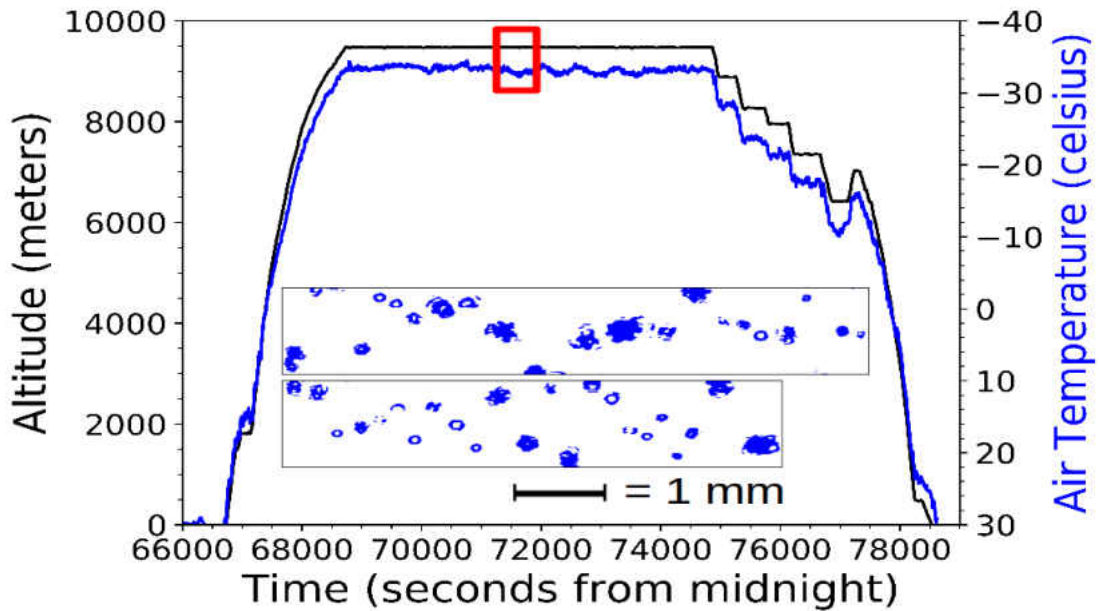


Figure 5: Plot showing the altitude (black) and air temperature (blue) sampled during the North Dakota Citation II Research Aircraft's flight on 31 July 2015 (-35 °C case). Measurements focused on high altitude anvil cirrus clouds produced by intense convection. The red rectangle indicates the time segment (71,710 – 71,770 s from midnight UTC) analyzed, where the average altitude is 9,475 m GPS and the average temperature is -35 °C. The center panels contain 2D-S images from the analyzed time.

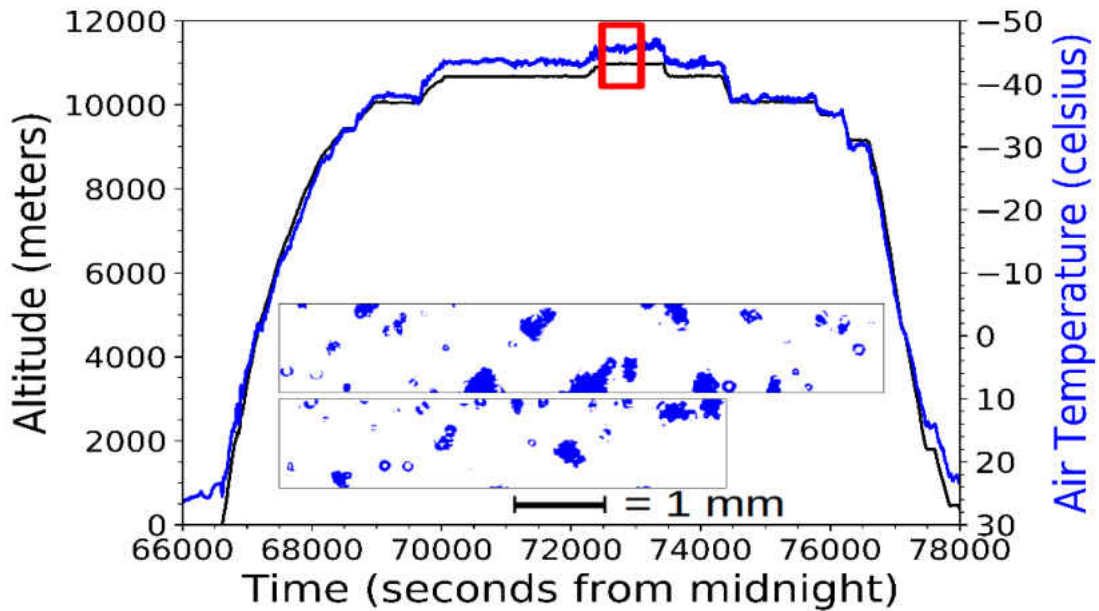


Figure 6: Plot showing the altitude (black) and air temperature (blue) sampled during the North Dakota Citation II Research Aircraft's flight on 01 August 2015 (-45 °C case). Measurements focused on high altitude anvil cirrus clouds produced by intense convection. The red rectangle indicates the time segment (72,700 – 72,760 s from midnight UTC) analyzed, where the average altitude is 11,000 m GPS and the average temperature is -45 °C. The center panels contain 2D-S images from the analyzed time.

## CHAPTER 6

### RESULTS AND DISCUSSION

The +10 °C case in Figure 7 shows strong agreement between the backscatter coefficients ( $\beta_{ECP}$  and  $\beta_{OID}$ ), with all times being within one standard deviation. At time 69,540 sfm there is the most disagreement, which is a difference of  $2.5 \times 10^{-3} \text{ m}^{-1} \text{ sr}^{-1}$ . When there is disagreement,  $\beta_{ECP}$  is consistently lower than  $\beta_{OID}$ , indicating a negative bias. The +5 °C case in Figure 8 has more variation between  $\beta_{ECP}$  and  $\beta_{OID}$  with no times of full agreement. In the +5 °C case,  $\beta_{ECP}$  is consistently lower than  $\beta_{OID}$  with disagreement reaching as high as approximately  $2.0 \times 10^{-3} \text{ m}^{-1} \text{ sr}^{-1}$  at time 57,880 sfm. At their peak difference,  $\beta_{ECP}$  is 50 % of  $\beta_{OID}$ , extending beyond the uncertainty by at least two standard deviations. The consistency at which  $\beta_{ECP}$  is lower than  $\beta_{OID}$  indicates there is a bias influencing the results. The -35 °C case in Figure 9 shows agreement within one standard deviation (see Eq. 6) between  $\beta_{ECP}$  and  $\beta_{OID}$  from time 71,710 sfm until time 71,740 sfm when they diverge with a difference up to approximately  $6.0 \times 10^{-4} \text{ m}^{-1} \text{ sr}^{-1}$  at time 71,750 sfm, or 50 % of the value given by the  $\beta_{ECP}$  at that time of 71,743 sfm.  $\beta_{OID}$  is consistently lower than  $\beta_{ECP}$  after time 71,743 sfm, alternating between one and three  $\beta_{ECP}$  standard deviations apart. The -45 °C case in Figure 10 contained the largest differences between  $\beta_{ECP}$  and  $\beta_{OID}$ , with disagreement reaching as high as 100 % of the OID value. The consistency of the variation indicates a positive bias.  $\beta_{OID}$  is beyond three standard deviations of the uncertainty of  $\beta_{ECP}$ , indicating disagreement. Figures 7, 8, 9, and 10 also show the derived backscatter and OID backscatter compared to the total wa-

ter content of the Nevzorov Probe in the lower right corner. The +5 °C, -35 °C, and -45 °C cases all show strong correlation with the trends of the total water content. The +10 °C shows much higher variability which is likely due to the OID receiver being saturated with power. Correlation between the total water content and the backscatter coefficients can also be seen in Figures 11 and 12. The minimal scatter in the total water content versus backscatter coefficients plots in Figures 7 through 12 indicates that the backscatter coefficient is an acceptable proxy for the total water content.

Under calculation of  $\beta_{ECP}$  compared to the OID for the +10 °C and +5 °C may be the result of multiple scattering occurring with the water droplets due to high concentrations. The OID may be receiving light scattered multiple times from the sides of the droplets rather than what was strictly scattered backward. Over calculation of  $\beta_{ECP}$  with ice cases is in part due to oversizing caused by the circle-fit method and irregularly shaped ice particles. As the circle fit represents each particle with a circle corresponding to the maximum width of the particle image, ice habits such as columns tend to be oversized. Future work could reduce the magnitude of this problem by using a diameter equivalent to the area of the particle's pixels. Where the circle-fit method creates a circle around particles and uses that diameter to represent the particle, the equivalent area diameter method removes blank pixels between the shadowed pixels and reduces the particle diameter accordingly. Ice habits which are highly irregular in their shape are most affected by which method of diameter sizing is used. As -35 °C case and -45 °C case both contained irregularly shaped particles, one sizing method over another will likely produce greatly different results. Another source of error for ice cases arises from forward scatter probes needing to be calibrated to account for the medium which is producing the forward scattering. The CDP included in CAPE2015 is calibrated for the scattering of liquid water droplets.

Encountering ice crystals therefore results in an inherent bias. In each case analyzed, the primary dependence of the backscatter coefficient is the particle concentration, with the particle size of secondary importance. Separate calculations of the concentration and sizing components of Eq. 6 showed that particle counting is the primary contributor to the uncertainty. The uncertainty related to particle counting can be reduced by using only environments which contain very large concentrations. The uncertainty related to sizing could be reduced in future work by decreasing the width of individual bins while covering the same particle size range. Thus, increasing the number of processed channels through the SODA software. Further deviation can be explained by sources of error not accountable in Eq. 6. The first is the fact that the backscatter efficiency produced by miepython is valid only for perfect  $180^\circ$  returns, where the OID receives light scattering from particles at a small range just above and below  $180^\circ$  (approximately  $179.75^\circ$  to  $180.25^\circ$ ). Another, less important, source of error results from refractive indices of both ice and water depending not only on the incident wavelength but on the temperature of the mediums as well (Wesely 1976). It can also be seen in Figures 9 and 10 that  $\beta_{ECP}$  has significantly more noise than  $\beta_{OID}$ . Added noise in  $\beta_{ECP}$  can be explained by the significantly smaller sampling volume sampled by the CDP, 2D-S, and HVPS3 compared to the OID. Future work can reduce this noise by averaging measurements over longer times.

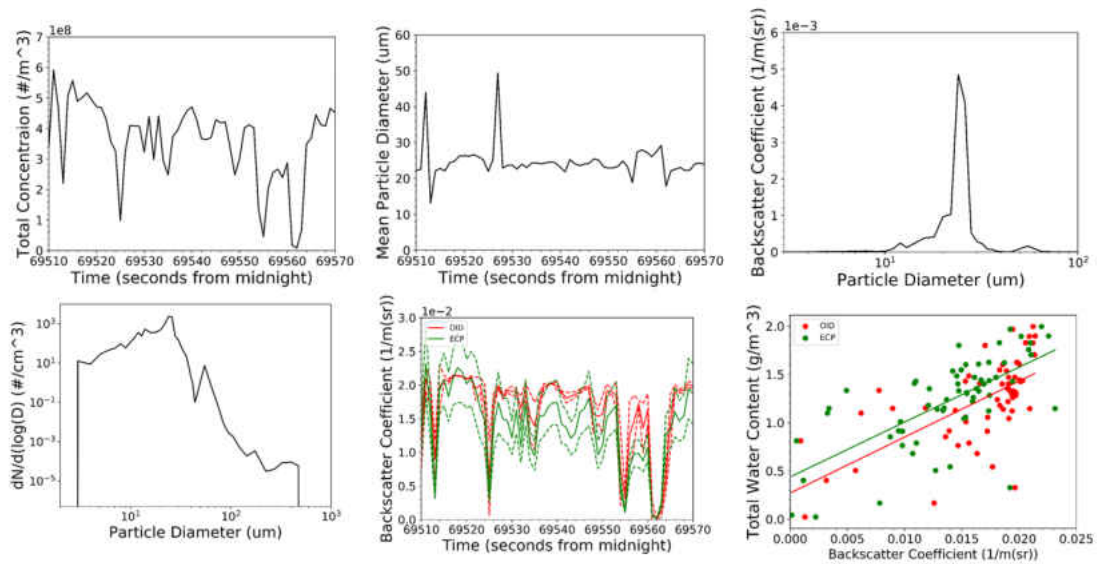


Figure 7: Plots showing results for the +10 °C case (15\_08.02.18\_23\_48). The probe measured total concentrations versus time can be seen in the upper left, the cloud probes measured mean particle diameter versus time in the upper center, the calculated backscatter coefficient versus the particle diameter in the upper right, the cloud probes measured particle size spectrum (normalized by bin width and particle diameter) in the lower left, the Optical Ice Detector (OID) measured backscatter coefficients with the derived backscatter coefficients versus time on the y-axis with corresponding calculated uncertainties in dashed lines in the lower center, and the Nevzorov Probe total water content versus the OID and derived backscatter coefficients with corresponding trend lines in the lower right.

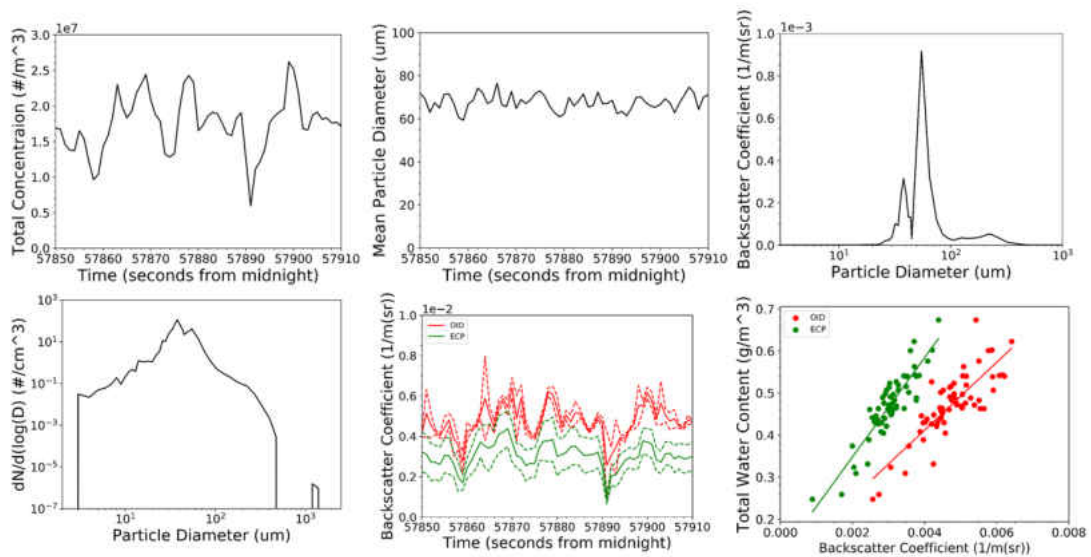


Figure 8: Plots showing results for the +5 °C case (15\_08\_01\_14\_37\_31). The probe measured total concentrations versus time can be seen in the upper left, the cloud probes measured mean particle diameter versus time in the upper center, the calculated backscatter coefficient versus the particle diameter in the upper right, the cloud probes measured particle size spectrum (normalized by bin width and particle diameter) in the lower left, the Optical Ice Detector (OID) measured backscatter coefficients with the derived backscatter coefficients versus time on the y-axis with corresponding calculated uncertainties in dashed lines in the lower center, and the Nevzorov Probe total water content versus the OID and derived backscatter coefficients with corresponding trend lines in the lower right.



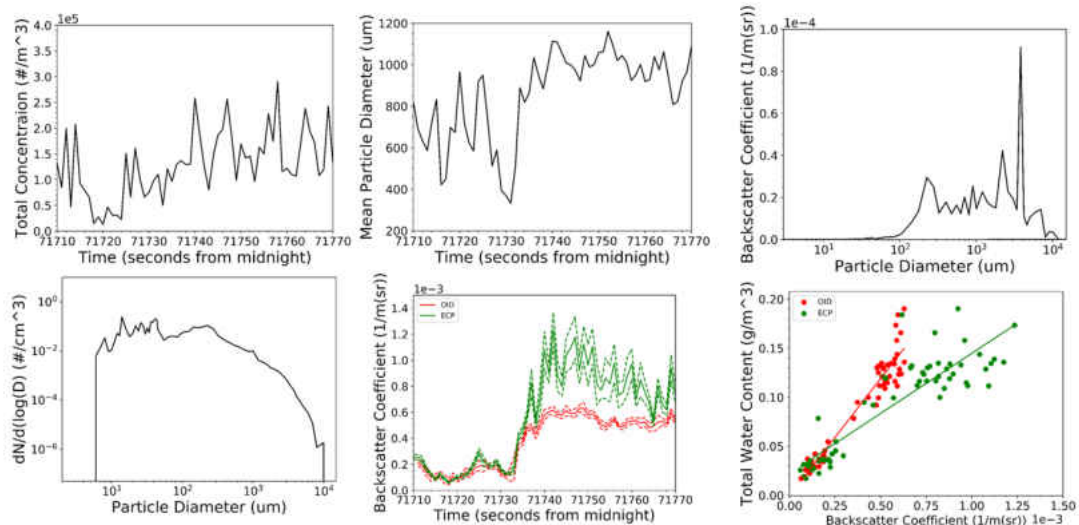


Figure 9: Plots showing results for the  $-35\text{ }^{\circ}\text{C}$  case (15.07.31\_18.18.35). The probe measured total concentrations versus time can be seen in the upper left, the cloud probes measured mean particle diameter versus time in the upper center, the calculated backscatter coefficient versus the particle diameter in the upper right, the cloud probes measured particle size spectrum (normalized by bin width and particle diameter) in the lower left, the Optical Ice Detector (OID) measured backscatter coefficients with the derived backscatter coefficients versus time on the y-axis with corresponding calculated uncertainties in dashed lines in the lower center, and the Nevzorov Probe total water content versus the OID and derived backscatter coefficients with corresponding trend lines in the lower right.

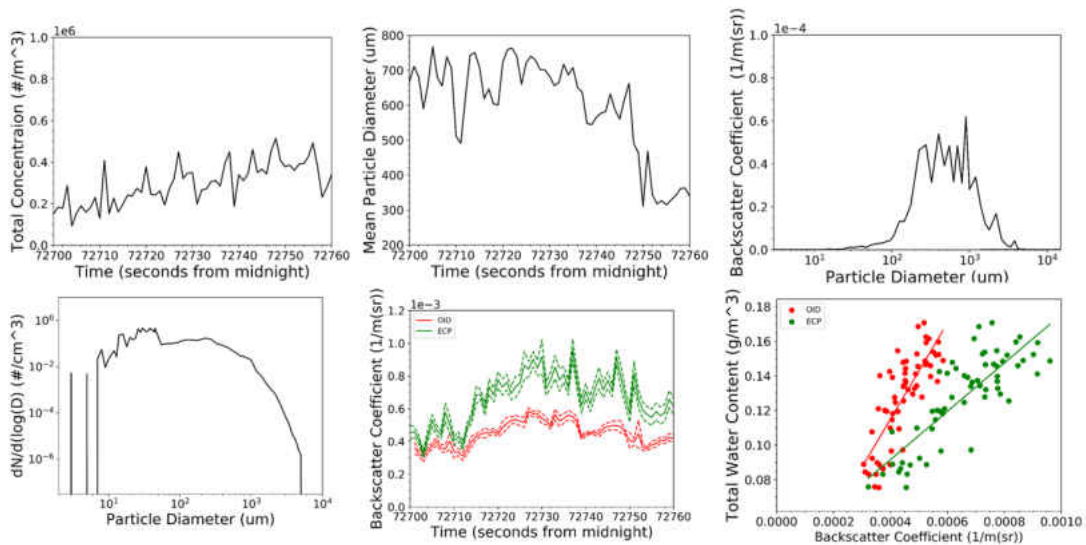


Figure 10: Plots showing results for the  $-45\text{ }^{\circ}\text{C}$  case (15\_08.01\_18\_20\_11). The probe measured total concentrations versus time can be seen in the upper left, the cloud probes measured mean particle diameter versus time in the upper center, the calculated backscatter coefficient versus the particle diameter in the upper right, the cloud probes measured particle size spectrum (normalized by bin width and particle diameter) in the lower left, the Optical Ice Detector (OID) measured backscatter coefficients with the derived backscatter coefficients versus time on the y-axis with corresponding calculated uncertainties in dashed lines in the lower center, and the Nevzorov Probe total water content versus the OID and derived backscatter coefficients with corresponding trend lines in the lower right.

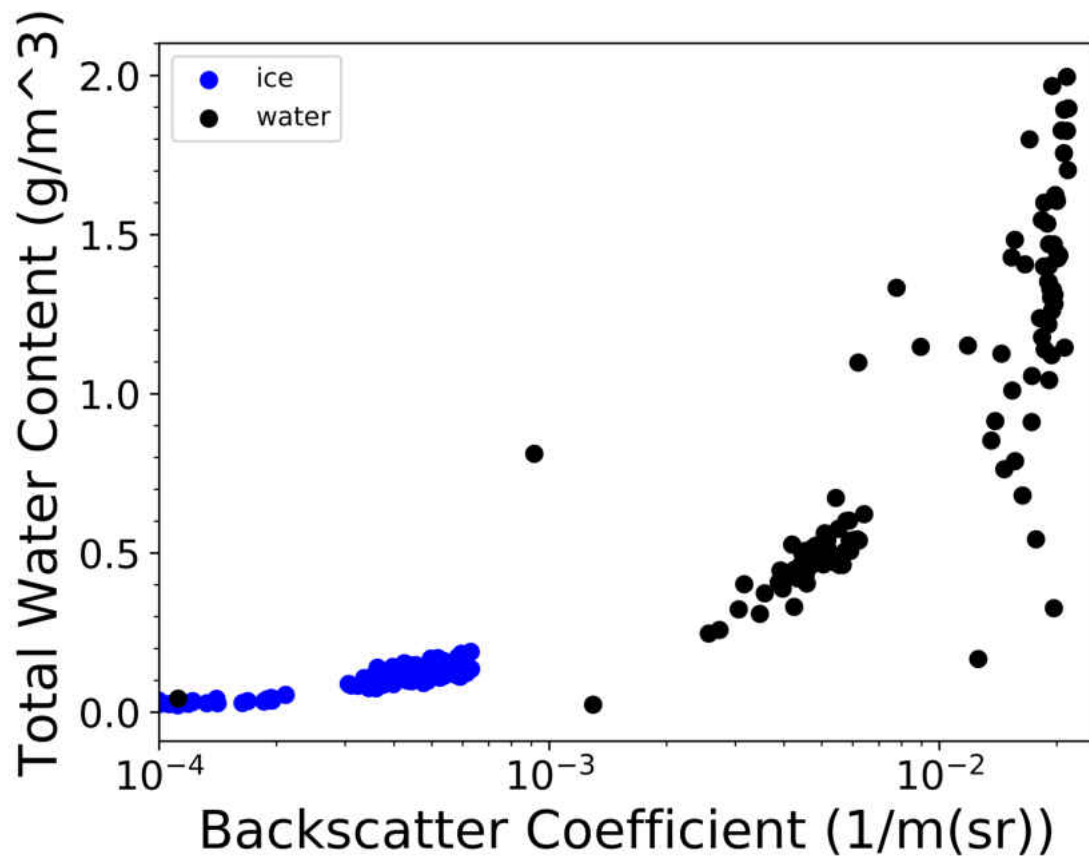


Figure 11: Plot showing the Nevzorov Probe total water content versus the Optical Ice Detector (OID) backscatter coefficients with a logarithmic x axis. The backscatter coefficients have been separated by water (black) and ice (blue) cases.

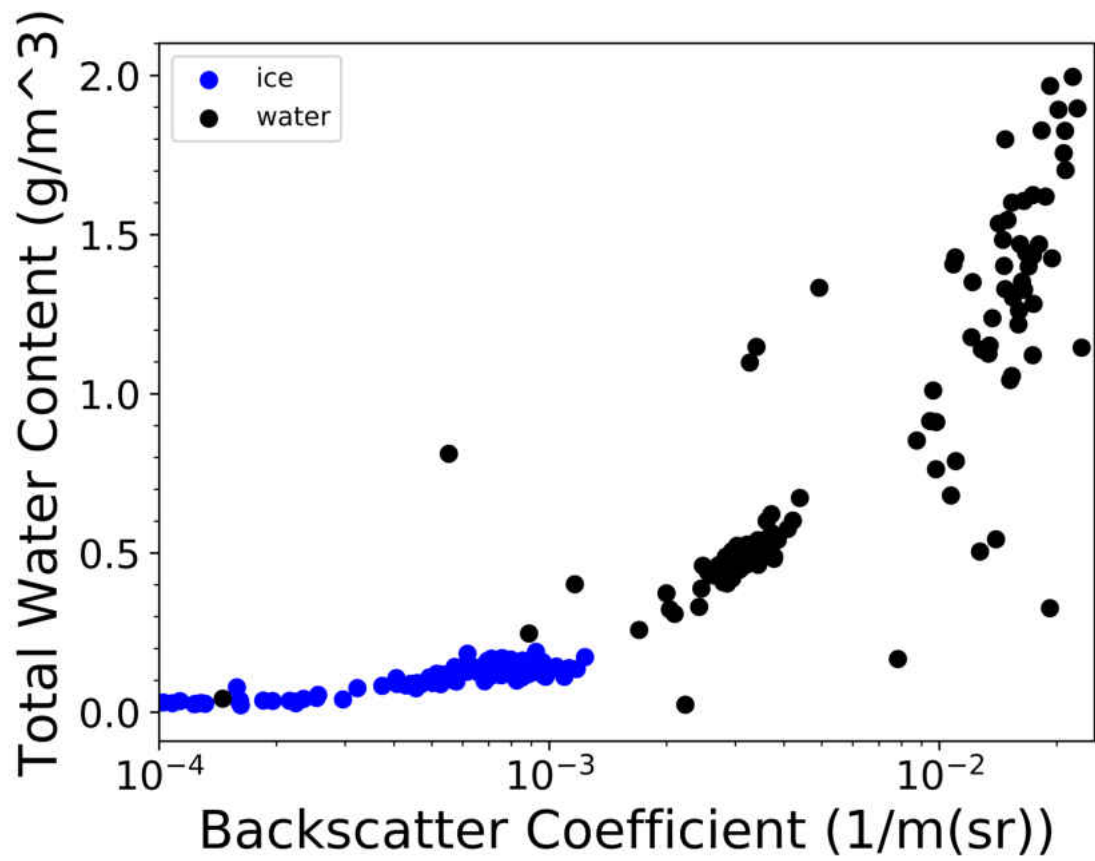


Figure 12: Plots showing the Nevzorov Probe total water content versus the derived backscatter coefficients with a logarithmic x axis. The backscatter coefficients have been separated by water (black) and ice (blue) cases.

## CHAPTER 7

### CONCLUSIONS

This work examined the difference between *in situ* lidar measured backscatter coefficients of cloud particles and backscatter coefficients derived from forward scattering probes and optical array probe data. It is found that the backscatter coefficient uncertainties are more highly dependent on particle concentration rather than size. While the derived backscatter coefficients are consistently higher than the OID backscatter coefficients for ice particle cases, indicating a positive bias, liquid water showed derived backscatter coefficients to be lower than the OID backscatter coefficients, indicating a negative bias. The derived backscatter coefficients are consistently two standard deviations or less from the OID backscatter coefficient, indicating agreement in three of the four cases. In all cases it was shown through comparisons with total water content that the backscatter coefficient is a suitable proxy for water content. This is a positive step toward understanding microphysically based backscatter calculation uncertainty and the use of airborne lidar for water content detection. Future work is still needed to perform verification in other environments, such as warmer temperatures/lower altitudes, expanding to larger data sets, examining higher or lower concentrations, and accounting for errors unique to forward scattering probes and optical array probes.

## APPENDIX A

Included in this appendix are the backscatter coefficient calculation results after using reconstruction processing. The +10 °C case in Figure 13 and +5 °C case in Figure 14 show nearly the same results as the All In processed data. The -35 °C case in Figure 15 consists of almost total agreement until 71,740 sfm, then disagreement within 1 standard deviation of the ECP data for the rest of the analyzed time. The -45 °C case in Figure 16 shows nearly total agreement between the ECP and OID data, with variation extending to only approximately one standard-deviation of ECP data at two points between 72,745 sfm and 72,755 sfm.

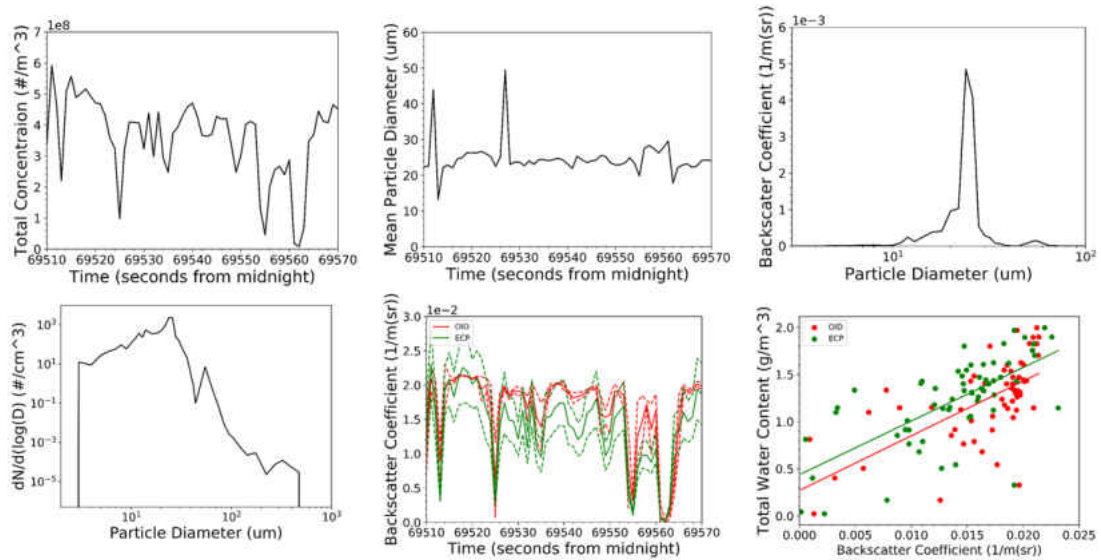


Figure 13: Plots showing results for the  $+10\text{ }^\circ\text{C}$  case (15\_08\_02\_18\_23\_48) using data processed with the Reconstruction method. The probe measured total concentrations versus time can be seen in the upper left, the cloud probes measured mean particle diameter versus time in the upper center, the calculated backscatter coefficient versus the particle diameter in the upper right, the cloud probes measured particle size spectrum (normalized by bin width and particle diameter) in the lower left, the Optical Ice Detector (OID) measured backscatter coefficients with the derived backscatter coefficients versus time on the y-axis with corresponding calculated uncertainties in dashed lines in the lower center, and the Nevzorov Probe total water content versus the OID and derived backscatter coefficients with corresponding trend lines in the lower right.

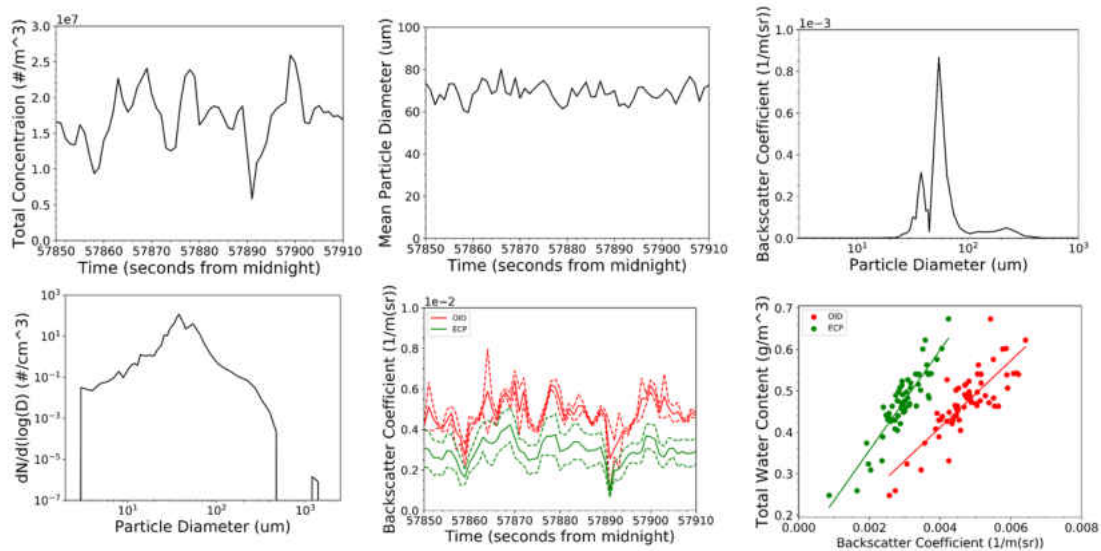


Figure 14: Plots showing results for the +5 °C case (15\_08\_01\_14\_37\_31) using data processed with the Reconstruction method. The probe measured total concentrations versus time can be seen in the upper left, the cloud probes measured mean particle diameter versus time in the upper center, the calculated backscatter coefficient versus the particle diameter in the upper right, the cloud probes measured particle size spectrum (normalized by bin width and particle diameter) in the lower left, the Optical Ice Detector (OID) measured backscatter coefficients with the derived backscatter coefficients versus time on the y-axis with corresponding calculated uncertainties in dashed lines in the lower center, and the Nevzorov Probe total water content versus the OID and derived backscatter coefficients with corresponding trend lines in the lower right.



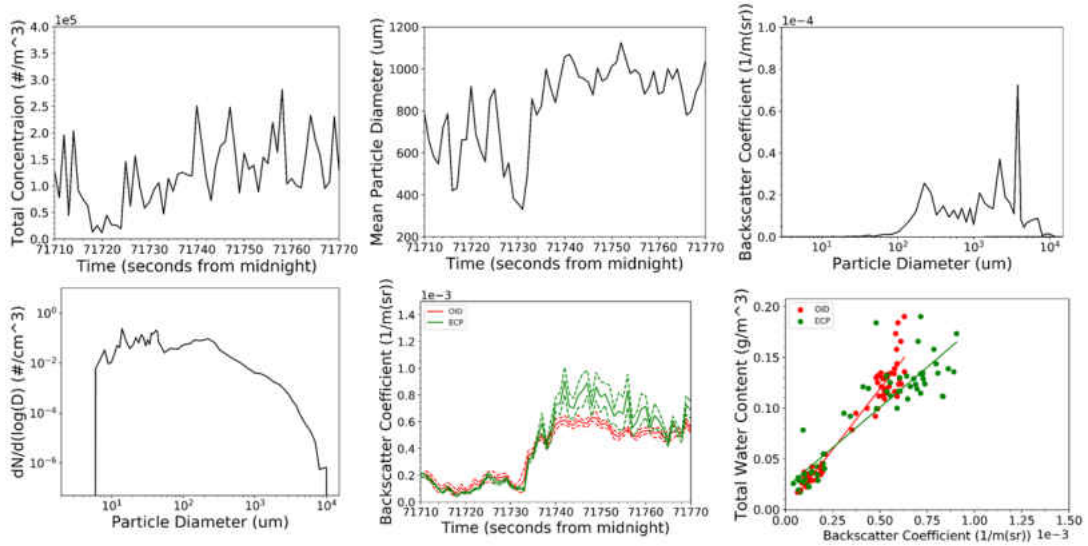


Figure 15: Plots showing results for the  $-35\text{ }^{\circ}\text{C}$  case (15\_07\_31\_18\_18.35) using data processed with the Reconstruction method. The probe measured total concentrations versus time can be seen in the upper left, the cloud probes measured mean particle diameter versus time in the upper center, the calculated backscatter coefficient versus the particle diameter in the upper right, the cloud probes measured particle size spectrum (normalized by bin width and particle diameter) in the lower left, the Optical Ice Detector (OID) measured backscatter coefficients with the derived backscatter coefficients versus time on the y-axis with corresponding calculated uncertainties in dashed lines in the lower center, and the Nevzorov Probe total water content versus the OID and derived backscatter coefficients with corresponding trend lines in the lower right.

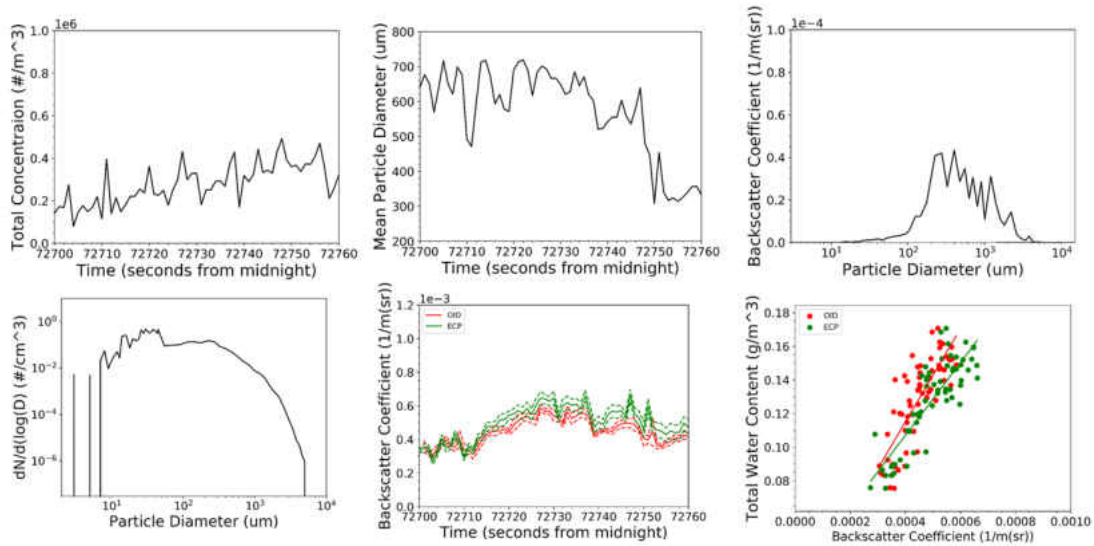


Figure 16: Plots showing results for the  $-45\text{ }^{\circ}\text{C}$  case (15\_08\_01\_18\_20\_11) using data processed with the Reconstruction method. The probe measured total concentrations versus time can be seen in the upper left, the cloud probes measured mean particle diameter versus time in the upper center, the calculated backscatter coefficient versus the particle diameter in the upper right, the cloud probes measured particle size spectrum (normalized by bin width and particle diameter) in the lower left, the Optical Ice Detector (OID) measured backscatter coefficients with the derived backscatter coefficients versus time on the y-axis with corresponding calculated uncertainties in dashed lines in the lower center, and the Nevzorov Probe total water content versus the OID and derived backscatter coefficients with corresponding trend lines in the lower right.

## REFERENCES

- Bailey, M. P., and J. Hallett, 2009: A Comprehensive Habit Diagram for Atmospheric Ice Crystals: Confirmation from the Laboratory, AIRS II, and Other Field Studies. *J. Atmos. Sci.*, **66**, 2888–2899, <https://doi.org/10.1175/2009JAS2883.1>.
- Baird, D. C., 1988: *Experimentation: An Introduction to Measurement Theory and Experiment Design*. 2nd edition. Prentice Hall, 193 pp.
- Bansemer, Aaron, 2013: Software for OAP Data Analysis Version 2. *Github*. <https://github.com/abansemer/soda2>.
- Beswick, K., D. Baumgardner, M. Gallagher, A. Volz-Thomas, P. Nedelec, K.-Y. Wang, and S. Lance, 2014: The backscatter cloud probe; a compact low-profile autonomous optical spectrometer. *Atmospheric Measurement Techniques*, **7**, 1443–1457, <https://doi.org/10.5194/amt-7-1443-2014>.
- Beswick, K., and Coauthors, 2015: Properties of Small Cirrus Ice Crystals from Commercial Aircraft Measurements and Implications for Flight Operations. *Tellus B: Chemical and Physical Meteorology*, **67**, 27876, <https://doi.org/10.3402/tellusb.v67.27876>.
- Bohren, C. F., and D. R. Huffman, 1983: *Absorption and scattering of light by small particles*. Wiley, xiv+530 pp.

- Delene, D. J., 2011: Airborne data processing and analysis software package. *Earth Sci Inform*, **4**, 29–44, <https://doi.org/10.1007/s12145-010-0061-4>.
- , K. Hibert, M. Poellot, and N. Brackin, 2019: The North Dakota Citation Research Aircraft Measurement Platform. *2019 SAE International Conference on Icing of Aircraft, Engines, and Structures*.
- Faber, S., J. R. French, and R. Jackson, 2018: Laboratory and in-flight evaluation of measurement uncertainties from a commercial Cloud Droplet Probe (CDP). *Atmos. Meas. Tech.*, **11**, 3645–3659, <https://doi.org/10.5194/amt-11-3645-2018>.
- Field, P. R., A. J. Heymsfield, and A. Bansemmer, 2006: Shattering and Particle Interarrival Times Measured by Optical Array Probes in Ice Clouds. *J. Atmos. Oceanic Technol.*, **23**, 1357–1371, <https://doi.org/10.1175/JTECH1922.1>.
- Halama, G., M. Ray, K. Anderson, M. Nesnidal, and R. Ide, 2010: Optical Ice Detection: Test Results from the NASA Glenn Icing Research Tunnel. *AIAA Atmospheric and Space Environments Conference*, American Institute of Aeronautics and Astronautics.
- Heymsfield, A. J., and J. L. Parrish, 1978: A Computational Technique for Increasing the Effective Sampling Volume of the PMS Two-Dimensional Particle Size Spectrometer. *J. Appl. Meteor.*, **17**, 1566–1572, [https://doi.org/10.1175/1520-0450\(1978\)017<1566:ACTFIT>2.0.CO;2](https://doi.org/10.1175/1520-0450(1978)017<1566:ACTFIT>2.0.CO;2).
- Horvath, H., R. L. Gunter, and S. W. Wilkison, 1990: Determination of the Coarse Mode of the Atmospheric Aerosol Using Data from a Forward-Scattering Spectrometer Probe. *Aerosol Science and Technology*, **12**, 964–980, <https://doi.org/10.1080/02786829008959407>.

- Hulst, H. C. van de, 1981: *Light Scattering by Small Particles*. Corrected Edition edition. Dover Publications, 496 pp.
- Jaffey, A. H., 1954: Solid Angle Subtended by a Circular Aperture at Point and Spread Sources: Formulas and Some Tables. *Review of Scientific Instruments*, **25**, 349–354, <https://doi.org/10.1063/1.1771061>.
- Jensen, M. P., and Coauthors, 2015: The Midlatitude Continental Convective Clouds Experiment (MC3E). *Bull. Amer. Meteor. Soc.*, **97**, 1667–1686, <https://doi.org/10.1175/BAMS-D-14-00228.1>.
- Kedenburg, S., M. Vieweg, T. Gissibl, and H. Giessen, 2012: Linear refractive index and absorption measurements of nonlinear optical liquids in the visible and near-infrared spectral region. *Opt. Mater. Express, OME*, **2**, 1588–1611, <https://doi.org/10.1364/OME.2.001588>.
- Korolev, A., 2007: Reconstruction of the Sizes of Spherical Particles from Their Shadow Images. Part I: Theoretical Considerations. *J. Atmos. Oceanic Technol.*, **24**, 376–389, <https://doi.org/10.1175/JTECH1980.1>.
- , and G. A. Isaac, 2005: Shattering during Sampling by OAPs and HVPS. Part I: Snow Particles. *J. Atmos. Oceanic Technol.*, **22**, 528–542, <https://doi.org/10.1175/JTECH1720.1>.
- Korolev, A., J. W. Strapp, G. A. Isaac, and E. Emery, 2013a: Improved Airborne Hot-Wire Measurements of Ice Water Content in Clouds. *J. Atmos. Oceanic Technol.*, **30**, 2121–2131, <https://doi.org/10.1175/JTECH-D-13-00007.1>.
- Korolev, A. V., J. W. Strapp, G. A. Isaac, and A. N. Nevzorov, 1998: The Nevzorov Airborne Hot-Wire LWC–TWC Probe: Principle of Operation

- and Performance Characteristics. *J. Atmos. Oceanic Technol.*, **15**, 1495–1510, [https://doi.org/10.1175/1520-0426\(1998\)015<1495:TNAHWLj2.0.CO;2](https://doi.org/10.1175/1520-0426(1998)015<1495:TNAHWLj2.0.CO;2).
- , G. A. Isaac, and J. Hallett, 1999: Ice particle habits in Arctic clouds. *Geophysical Research Letters*, **26**, 1299–1302, <https://doi.org/10.1029/1999GL900232>.
- , E. F. Emery, J. W. Strapp, S. G. Cober, and G. A. Isaac, 2013b: Quantification of the Effects of Shattering on Airborne Ice Particle Measurements. *J. Atmos. Oceanic Technol.*, **30**, 2527–2553, <https://doi.org/10.1175/JTECH-D-13-00115.1>.
- Kumjian, M. R., S. Mishra, S. E. Giangrande, T. Toto, A. V. Ryzhkov, and A. Bansemer, 2016: Polarimetric radar and aircraft observations of saggy bright bands during MC3E. *Journal of Geophysical Research: Atmospheres*, **121**, 3584–3607, <https://doi.org/10.1002/2015JD024446>.
- Lance, S., C. A. Brock, D. Rogers, and J. A. Gordon, 2010: Water droplet calibration of the Cloud Droplet Probe (CDP) and in-flight performance in liquid, ice and mixed-phase clouds during ARCPAC. *Atmospheric Measurement Techniques*, **3**, 1683–1706, <https://doi.org/10.5194/amt-3-1683-2010>.
- Lawson, R. P., B. A. Baker, C. G. Schmitt, and T. L. Jensen, 2001: An overview of microphysical properties of Arctic clouds observed in May and July 1998 during FIRE ACE. *Journal of Geophysical Research: Atmospheres*, **106**, 14989–15014, <https://doi.org/10.1029/2000JD900789>.
- , D. O’Connor, P. Zmarzly, K. Weaver, B. Baker, Q. Mo, and H. Jonsson, 2006: The 2D-S (Stereo) Probe: Design and Preliminary Tests of a New Airborne, High-Speed, High-Resolution Particle Imaging Probe. *J. Atmos. Oceanic Technol.*, **23**, 1462–1477, <https://doi.org/10.1175/JTECH1927.1>.

- Liou, K.-N., and P. Yang, 2016: Light Scattering by Ice Crystals by Kuo-Nan Liou. *Cambridge Core*, <https://doi.org/10.1017/CBO9781139030052>.
- Mason, J., W. Strapp, and P. Chow, 2006: The Ice Particle Threat to Engines in Flight. *44th AIAA Aerospace Sciences Meeting and Exhibit*, Reno, Nevada, American Institute of Aeronautics and Astronautics.
- McFarquhar, G. M., and Coauthors, 2017: Processing of Ice Cloud In Situ Data Collected by Bulk Water, Scattering, and Imaging Probes: Fundamentals, Uncertainties, and Efforts toward Consistency. *Meteorological Monographs*, **58**, 11.1-11.33, <https://doi.org/10.1175/AMSMONOGRAPHS-D-16-0007.1>.
- O'Shea, S. J., J. Crosier, J. Dorsey, W. Schledewitz, I. Crawford, S. Borrmann, R. Cotton, and A. Bansemer, 2019: Revisiting particle sizing using greyscale optical array probes: evaluation using laboratory experiments and synthetic data. *Atmospheric Measurement Techniques*, **12**, 3067–3079, <https://doi.org/10.5194/amt-12-3067-2019>.
- Prahl, S., 2019: *Github*. <https://github.com/scottprahl/miepython/> (Accessed October 22, 2019)
- Ray, M., and K. Anderson, 2015: Analysis of Flight Test Results of the Optical Ice Detector. *SAE Int. J. Aerosp.*, **8**, 1–8, <https://doi.org/10.4271/2015-01-2106>.
- , M. Nesnidal, and D. Socha, 2009: Optical Detection of Airborne Ice Crystals and Liquid Water Droplets. *1st AIAA Atmospheric and Space Environments Conference*, American Institute of Aeronautics and Astronautics.
- Schmidt, J. M., and Coauthors, 2019: Radar Detection of Individual Raindrops. *Bull. Amer. Meteor. Soc.*, <https://doi.org/10.1175/BAMS-D-18-0130.1>.

- Schnaiter, M., E. Järvinen, A. Abdelmonem, and T. Leisner, 2018: PHIPS-HALO: the airborne particle habit imaging and polar scattering probe; Part 2: Characterization and first results. *Atmospheric Measurement Techniques*, **11**, 341–357, <https://doi.org/10.5194/amt-11-341-2018>.
- Schön, R., and Coauthors, 2011: Particle Habit Imaging Using Incoherent Light: A First Step toward a Novel Instrument for Cloud Microphysics. *J. Atmos. Oceanic Technol.*, **28**, 493–512, <https://doi.org/10.1175/2011JTECHA1445.1>.
- Skofronick-Jackson, G., and Coauthors, 2014: Global Precipitation Measurement Cold Season Precipitation Experiment (GCPEX): For Measurement’s Sake, Let It Snow. *Bull. Amer. Meteor. Soc.*, **96**, 1719–1741, <https://doi.org/10.1175/BAMS-D-13-00262.1>.
- Warren, S. G., and R. E. Brandt, 2008: Optical constants of ice from the ultraviolet to the microwave: A revised compilation. *Journal of Geophysical Research: Atmospheres*, **113**, <https://doi.org/10.1029/2007JD009744>.
- Wesely, M. L., 1976: The Combined Effect of Temperature and Humidity Fluctuations on Refractive Index. *J. Appl. Meteor.*, **15**, 43–49, [https://doi.org/10.1175/1520-0450\(1976\)015<0043:TCEOTA>2.0.CO;2](https://doi.org/10.1175/1520-0450(1976)015<0043:TCEOTA>2.0.CO;2).
- Westbrook, C., R. Hogan, E. O’Connor, and A. Illingworth, 2010: Estimating drizzle drop size and precipitation rate using two-colour lidar measurements. *Atmospheric Measurement Techniques*, **3**, <https://doi.org/10.5194/amtd-3-891-2010>.
- Wu, W., and G. M. McFarquhar, 2016: On the Impacts of Different Definitions of Maximum Dimension for Nonspherical Particles Recorded by 2D Imaging Probes. *J. Atmos. Oceanic Technol.*, **33**, 1057–1072, <https://doi.org/10.1175/JTECH-D-15-0177.1>.



Yau, M. K., and R. R. Rogers, 1989: *A Short Course in Cloud Physics*. 3 edition.  
Butterworth-Heinemann, 304 pp.

Zhang, F., J. Pyle, and G. R. North, 2015: *Encyclopedia of Atmospheric Sciences*.  
Academic Press.

OID Analysis. *SourceForge*. <https://sourceforge.net/projects/oid-analysis/> (Accessed  
October 22, 2019)